

Accelerating Ordered Subsets Image Reconstruction for X-ray CT Using Spatially Nonuniform Optimization Transfer

Donghwan Kim*, *Student Member, IEEE*, Debashish Pal, *Member, IEEE*, Jean-Baptiste Thibault, *Member, IEEE*, and Jeffrey A. Fessler, *Fellow, IEEE*

Abstract—Statistical image reconstruction algorithms in X-ray computed tomography (CT) provide improved image quality for reduced dose levels but require substantial computation time. Iterative algorithms that converge in few iterations and that are amenable to massive parallelization are favorable in multi-processor implementations. The separable quadratic surrogate (SQS) algorithm is desirable as it is simple and updates all voxels simultaneously. However, the standard SQS algorithm requires many iterations to converge. This paper proposes an extension of the SQS algorithm that leads to *spatially nonuniform updates*. The nonuniform (NU) SQS encourages larger step sizes for the voxels that are expected to change more between the current and the final image, accelerating convergence, while the derivation of NU-SQS guarantees monotonic descent. Ordered subsets (OS) algorithms can also accelerate SQS, provided suitable “subset balance” conditions hold. These conditions can fail in 3-D helical cone-beam CT due to incomplete sampling outside the axial region-of-interest (ROI). This paper proposes a modified OS algorithm that is more stable outside the ROI in helical CT. We use CT scans to demonstrate that the proposed NU-OS-SQS algorithm handles the helical geometry better than the conventional OS methods and “converges” in less than half the time of ordinary OS-SQS.

Index Terms—Computed tomography (CT), ordered subsets (OS), parallelizable iterative algorithms, separable quadratic surrogates, statistical image reconstruction.

I. INTRODUCTION

STATISTICAL image reconstruction methods can improve resolution and reduce noise and artifacts by minimizing either penalized likelihood (PL) [1]–[3] or penalized weighted least-squares (PWLS) [4]–[6] cost functions that model the

physics and statistics in X-ray computed tomography (CT). The primary drawback of these methods is their computationally expensive iterative algorithms. This paper describes new accelerated minimization algorithms for X-ray CT statistical image reconstruction.

There are several iterative algorithms for X-ray CT. Coordinate descent (CD) algorithms [7] (also known as Gauss Siedel algorithms [8, p. 507]) and block/group coordinate descent (BCD/GCD) algorithms [9]–[11], update one or a group of voxels sequentially. These can converge in few iterations but can require long computation time per iteration [6], [12]. Considering modern computing architectures, algorithms that update all voxels simultaneously and that are amenable to parallelization are desirable, such as ordered subsets based on separable quadratic surrogate (OS-SQS) [13]–[15] and preconditioned conjugate gradient (PCG) algorithms [16]. However, those highly parallelizable algorithms require more iterations than CD algorithms [6], [12], and thus it is desirable to reduce the number of iterations needed to reach acceptable images. Splitting techniques [17] can accelerate convergence [18], but require substantial extra memory.

In this paper, we propose an enhanced version of a highly parallelizable SQS algorithm that accelerates convergence. SQS algorithms are optimization transfer methods that replace the original cost function by a simple surrogate function [19], [20]. Here, we construct surrogates with spatially *nonuniform* curvatures that provide spatially *nonuniform* step sizes to accelerate convergence.

Spatially nonhomogeneous (NH) approach [7] accelerated the CD algorithm by more frequently visiting the voxels that need updates. This approach is effective because the differences between the initial and final images are nonuniform. Inspired by such ideas, we propose a spatially nonuniform (NU) optimization transfer method that encourages larger updates for voxels that are predicted to be farther from the optimal value, using De Pierro’s idea in SQS [21]. We provide a theoretical justification for the acceleration of NU method by analyzing the convergence rate of SQS algorithm (in Section II-D). The NH approach also balanced homogeneous and nonhomogeneous updates for fast overall convergence rate [7]. Section III-C discusses similar considerations for the proposed NU approach.

OS, also known as incremental gradient methods [22], [23] or block iterative methods [24], can accelerate gradient-based algorithms by grouping the projection data into (ordered) subsets and updating the image using each subset. OS algorithms are

Manuscript received March 16, 2013; revised May 24, 2013; accepted May 27, 2013. Date of publication June 07, 2013; date of current version October 28, 2013. This work was supported in part by GE Healthcare, in part by the National Institutes of Health under Grant R01-HL-098686, and equipment donations from Intel. *Asterisk indicates corresponding author.*

This paper has supplementary downloadable materials available at <http://ieeexplore.ieee.org>, provided by the author.

D. Kim is with the Department of Electrical Engineering and Computer Science, University of Michigan, Ann Arbor, MI 48105 USA (e-mail: kimdongh@umich.edu).

D. Pal and J.-B. Thibault are with the GE Healthcare Technologies, Waukesha, WI 53188 USA (e-mail: debashish.pal@ge.com; jean-baptiste.thibault@med.ge.com).

J. A. Fessler is with the Department of Electrical Engineering and Computer Science, University of Michigan, Ann Arbor, MI 48105 USA (e-mail: fessler@umich.edu).

Color versions of one or more of the figures in this paper are available online at <http://ieeexplore.ieee.org>.

Digital Object Identifier 10.1109/TMI.2013.2266898

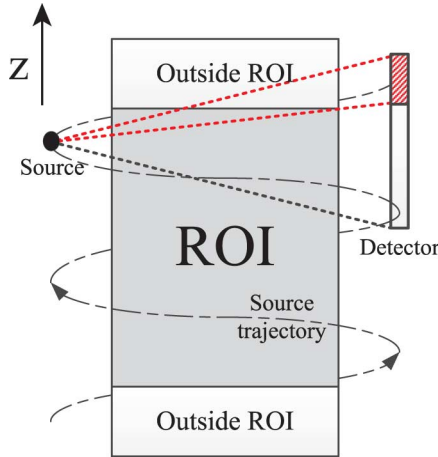


Fig. 1. Diagram of helical CT geometry. A (red) dashed region indicates the detector rows that measure data with contributions from voxels both within and outside the ROI.

most effective when a properly scaled gradient of each subset data-fit term approximates the gradient of the full data-fidelity term, and then it can accelerate convergence by a factor of the number of subsets. However, standard OS algorithms usually approach a limit-cycle where the sub-iterations loop around the optimal point. OS algorithms can be modified so that they converge by introducing relaxation [25], reducing the number of subsets, or by using incremental optimization transfer methods [26]. Unfortunately, such methods converge slower than ordinary OS algorithms in early iterations. Therefore, we investigated averaging the sub-iterations when the algorithm reaches a limit-cycle, which improves image quality without slowing convergence. (There was a preliminary simulation study of this idea in [27].)

In cone-beam CT, the user must define a region-of-interest (ROI) along the axial (z) direction for image reconstruction (see Fig. 1). Model-based reconstruction methods for cone-beam CT should estimate many voxels outside the ROI, because parts of each patient usually lie outside the ROI yet contribute to some measurements. However, accurately estimating non-ROI voxels is difficult since they are incompletely sampled, which is called the “long-object problem” [28]. Reconstructing the non-ROI voxels adequately is important, as they may impact the estimates within the ROI. Unfortunately in OS algorithms, the sampling of these extra slices leads to very imbalanced subsets particularly for large number of subsets, which can destabilize OS algorithm outside the ROI. This paper proposes an improved OS algorithm that is more stable for 3-D helical CT by defining better scaling factors for the subset-based gradient [29].

The paper is organized as follows. Section II reviews PL and PWLS problems for X-ray CT image reconstruction. We review the optimization transfer methods including the SQS algorithm and analyze its convergence rate. Section III presents the proposed spatially nonuniform SQS algorithm (NU-SQS). Section IV reviews the standard OS algorithm and refines it for 3-D helical CT. Section V shows the experimental results on various data sets, quantifying the convergence rate and reconstructed image quality. Finally, Section VI offers conclusions. The results show that the NU approach more than doubles the

convergence rate, and the improved OS algorithm provides acceptable images in helical CT.

II. STATISTICAL IMAGE RECONSTRUCTION

A. Problem

We reconstruct a nonnegative image $x = (x_1, \dots, x_{N_p}) \in \mathbb{R}_+^{N_p}$ from noisy measured transmission data $Y \in \mathbb{R}^{N_d}$ by minimizing either PL or PWLS cost functions

$$\hat{x} = \arg \min_{x \geq 0} \Psi(x) \quad (1)$$

$$\begin{aligned} \Psi(x) &\triangleq L(x) + R(x) \\ &= \sum_{i=1}^{N_d} h_i([Ax]_i) + \sum_{k=1}^{N_r} \psi_k([Cx]_k) \end{aligned} \quad (2)$$

where \hat{x} is a minimizer of $\Psi(x)$ subject to a nonnegativity constraint. The function $L(x)$ is a negative log-likelihood term (data-fit term) and $R(x)$ is a regularizer. The matrix $A = \{a_{ij}\}$ is a projection operator ($a_{ij} \geq 0$ for all i, j) where $[Ax]_i \triangleq \sum_{j=1}^{N_p} a_{ij}x_j$, and $C = \{c_{kj}\}$ is a finite differencing matrix considering 26 neighboring voxels in 3-D image space.¹ The function $\psi_k(t)$ is a (convex and typically nonquadratic) edge-preserving potential function. The function $h_i(t)$ is selected based on the chosen statistics and physics.

- PL for pre-log data Y_i with Poisson model [1]–[3] uses

$$h_i(t) = (b_i e^{-t} + r_i) - Y_i \log(b_i e^{-t} + r_i) \quad (3)$$

where b_i is the blank scan factor and r_i is the mean number of background events. The function $h_i(\cdot)$ is nonconvex if $r_i \neq 0$, or convex otherwise. A shifted Poisson model [30] that partially accounts for electronic recorded noise can be used instead.

- PWLS for post-log data $y_i = \log(b_i/(Y_i - r_i))$ with Gaussian model [4]–[6] uses a convex quadratic function

$$h_i(t) = \frac{1}{2} w_i (t - y_i)^2 \quad (4)$$

where $w_i = (Y_i - r_i)^2 / Y_i$ provides statistical weighting. We use the PWLS cost function for our experiments in Sections IV and V.

The proposed NU-SQS algorithm, based on optimization transfer methods (in Section II-B), decreases the cost function $\Psi(x)$ monotonically for either (3) or (4).

B. Optimization Transfer Method

When a cost function $\Psi(x)$ is difficult to minimize, we replace $\Psi(x)$ with a surrogate function $\phi^{(n)}(x)$ at the n th iteration for computational efficiency. This method is called optimization transfer [19], [20], which is also known as a majorization principle [31], and a comparison function [32]. There are many optimization transfer algorithms such as expectation maximization (EM) algorithms [33], [34], separable surrogate algorithms

¹Each row of C consists of a permutation of $(1, -1, 0, \dots, 0) \in \mathbb{R}^{N_p}$ where the indexes of the nonzero entries 1 and -1 corresponds to adjacent voxel locations in 3-D image space.

based on De Pierro's lemma [35]–[37] and surrogate algorithms using Lipschitz constants [38], [39].

The basic iteration of an optimization transfer method is

$$x^{(n+1)} = \arg \min_{x \geq 0} \phi^{(n)}(x). \quad (5)$$

To monotonically decrease $\Psi(x)$, we design surrogate functions $\phi^{(n)}(x)$ that satisfy the following majorization conditions:

$$\begin{aligned} \Psi(x^{(n)}) &= \phi^{(n)}(x^{(n)}) \\ \Psi(x) &\leq \phi^{(n)}(x), \quad \forall x \in \mathbb{R}_+^{N_p}. \end{aligned} \quad (6)$$

Constructing surrogates with smaller curvatures while satisfying condition (6) is the key to faster convergence in optimization transfer methods [11].

Optimization transfer has been used widely in tomography problems. De Pierro developed a separable surrogate (SS) approach in emission tomography [35], [36]. Quadratic surrogate (QS) functions have been derived for nonquadratic problems, enabling monotonic descent [1]. SQS algorithms combine SS and QS [14], and are the focus of this paper. Partitioned SQS methods for multi-core processors have been proposed for separating the image domain by the number of processors and updating each of them separately while preserving the monotonicity [40]. In addition, replacing $\mathbb{R}_+^{N_p}$ in (6) by an interval that is known to include the minimizer \hat{x} can reduce the surrogate curvature [7], [41].

Building on this history of optimization transfer methods that seek simple surrogates with small curvatures, we propose a *spatially nonuniform* SQS (NU-SQS) algorithm that satisfies condition (6) and converges faster than the standard SQS. We review the derivation of the SQS algorithm next.

C. Separable Quadratic Surrogate Algorithm

We first construct a quadratic surrogate at the n th iteration for the nonquadratic cost function in (2)

$$\Psi(x) = L(x) + R(x) \leq Q_L^{(n)}(x) + Q_R^{(n)}(x) \quad (7)$$

where $Q_L^{(n)}(x)$ and $Q_R^{(n)}(x)$ are quadratic surrogates for $L(x)$ and $R(x)$. Based on (2), the quadratic surrogate for $L(x)$ has the form

$$\begin{aligned} Q_L^{(n)}(x) &= \sum_{i=1}^{N_d} q_i^{(n)}([Ax]_i) \\ q_i^{(n)}(t) &\triangleq h_i(t_i^{(n)}) + \check{c}_i^{(n)}(t - t_i^{(n)}) \\ &\quad + \frac{\check{c}_i^{(n)}}{2}(t - t_i^{(n)})^2 \end{aligned} \quad (8)$$

where $t_i^{(n)} \triangleq [Ax^{(n)}]_i$, and $\check{c}_i^{(n)} = \max\{\check{c}_i^{(n)}, \eta\}$ is the curvature of $q_i^{(n)}(t)$ for some small positive value η that ensures the curvature $\check{c}_i^{(n)}$ positive [1]. In PWLS problem, $h_i(\cdot)$ is quadratic already, so $q_i^{(n)}(t) = h_i(t)$. The quadratic surrogate $Q_R^{(n)}(x)$ for $R(x)$ is defined similarly.

We choose curvatures $\{\check{c}_i^{(n)}\}$ that satisfy the monotonicity conditions in (6). For PL, the smallest curvatures

$$\check{c}_i^{(n)} \triangleq \begin{cases} \left[2 \frac{h_i(0) - h_i(t_i^{(n)}) + t_i^{(n)} \dot{h}_i(t_i^{(n)})}{[t_i^{(n)}]^2} \right]_+, & t_i^{(n)} > 0 \\ [\ddot{h}_i(0)]_+, & t_i^{(n)} = 0 \end{cases} \quad (9)$$

where $[t]_+ = \max\{t, 0\}$, called ‘‘optimal curvatures,’’ lead to the fastest convergence rate but require an extra back-projection each iteration for nonquadratic problems [1]. Alternatively, we may use ‘‘maximum curvatures.’’

$$\check{c}_i \triangleq \max_{t \geq 0} \ddot{h}_i(t) \quad (10)$$

that we can precompute before the first iteration [1].

Next, we generate a separable surrogate of the quadratic surrogate. For completeness, we repeat De Pierro's argument in [14]. We first rewrite forward projection $[Ax]_i$ as follows:

$$\begin{aligned} [Ax]_i &= \sum_{j=1}^{N_p} a_{ij} x_j \\ &= \sum_{\substack{j=1 \\ a_{ij} \neq 0}}^{N_p} \pi_{ij}^{(n)} \left(\frac{a_{ij}}{\pi_{ij}^{(n)}} (x_j - x_j^{(n)}) + [Ax^{(n)}]_i \right) \end{aligned} \quad (11)$$

where a nonnegative real number $\pi_{ij}^{(n)}$ is zero only if a_{ij} is zero for all i, j , and satisfies $\sum_{j=1}^{N_p} \pi_{ij}^{(n)} = 1$ for all i . Using the convexity of $q_i^{(n)}(\cdot)$ and the convexity inequality yields

$$q_i^{(n)}([Ax]_i) \leq \sum_{\substack{j=1 \\ a_{ij} \neq 0}}^{N_p} \pi_{ij}^{(n)} q_i^{(n)} \left(\frac{a_{ij}}{\pi_{ij}^{(n)}} (x_j - x_j^{(n)}) + [Ax^{(n)}]_i \right). \quad (12)$$

Thus, we have the following SQS $\phi_L^{(n)}(x)$ (with a diagonal Hessian) for the data-fit term $L(x)$

$$L(x) \leq Q_L^{(n)}(x) \leq \phi_L^{(n)}(x) \triangleq \sum_{j=1}^{N_p} \phi_{L,j}^{(n)}(x_j) \quad (13)$$

$$\phi_{L,j}^{(n)}(x_j) \triangleq \sum_{\substack{i=1 \\ a_{ij} \neq 0}}^{N_d} \pi_{ij}^{(n)} q_i^{(n)} \left(\frac{a_{ij}}{\pi_{ij}^{(n)}} (x_j - x_j^{(n)}) + [Ax^{(n)}]_i \right). \quad (14)$$

The second derivative (curvature) of the surrogate $\phi_{L,j}^{(n)}(x_j)$ is

$$d_j^{L,(n)} \triangleq \frac{\partial^2}{\partial x_j^2} \phi_{L,j}^{(n)}(x_j) = \sum_{\substack{i=1 \\ a_{ij} \neq 0}}^{N_d} \check{c}_i^{(n)} \frac{a_{ij}^2}{\pi_{ij}^{(n)}}. \quad (15)$$

We can define a SQS $\phi_{R,j}^{(n)}(x_j)$ for the regularizer similarly, and it has the curvature

$$d_j^{R,(n)} \triangleq \frac{\partial^2}{\partial x_j^2} \phi_{R,j}^{(n)}(x_j) = \sum_{\substack{k=1 \\ c_{kj} \neq 0}}^{N_r} \check{c}_k^{(n)} \frac{c_{kj}^2}{\pi_{kj}^{(n)}} \quad (16)$$

where $\pi_{kj}^{(n)}$ have similar constraints as $\pi_{ij}^{(n)}$, $\ddot{\psi}_k(0) = \max_t \ddot{\psi}_k(t)$ for maximum curvature [14], or $\dot{\psi}_k(0)$ can be replaced by $\dot{\psi}_k([Cx^{(n)}]_k)/[Cx^{(n)}]_k$ for Huber's optimal curvature [32, Lemma 8.3, p.184].

Combining the surrogates for the data-fit term and regularizer and minimizing it in (5) leads to the following SQS method [14] that updates all voxels simultaneously with a "denominator" $d_j^{(n)} \triangleq d_j^{L,(n)} + d_j^{R,(n)}$ as

$$x_j^{(n+1)} = \left[x_j^{(n)} - \frac{1}{d_j^{(n)}} \frac{\partial}{\partial x_j} \Psi(x^{(n)}) \right]_+ \quad (17)$$

where a clipping $[\cdot]_+$ enforces the nonnegativity constraint. This SQS decreases the cost function $\Psi(x)$ monotonically, and it converges based on the proof in [20]. If $\Psi(x)$ is convex, a sequence $\{x^{(n)}\}$ converges to $x^{(\infty)}$ that is a global minimizer \hat{x} . Otherwise, $\{x^{(n)}\}$ converges to a local minimizer $x^{(\infty)}$ which may or may not be a global minimizer \hat{x} depending on the initial image $x^{(0)}$.

The implementation and convergence rate of SQS depend on the choice of $\pi_{ij}^{(n)}$. A general form for $\pi_{ij}^{(n)}$ is

$$\pi_{ij}^{(n)} \triangleq \frac{\lambda_{ij}^{(n)}}{\sum_{\substack{l=1 \\ a_{il} \neq 0}}^{N_p} \lambda_{il}^{(n)}} \quad (18)$$

where a nonnegative real number $\lambda_{ij}^{(n)}$ is zero only if a_{ij} is zero. Then (15) can be rewritten as

$$d_j^{L,(n)} = \sum_{\substack{i=1 \\ a_{ij} \neq 0}}^{N_d} \check{c}_i^{(n)} \frac{a_{ij}^2}{\lambda_{ij}^{(n)}} \left(\sum_{\substack{l=1 \\ a_{il} \neq 0}}^{N_p} \lambda_{il}^{(n)} \right). \quad (19)$$

Summations involving the constraint $a_{ij} \neq 0$ require knowledge of the projection geometry, and thereby each summation can be viewed as a type of forward or back projection.

The standard choice [11], [14]

$$\bar{\lambda}_{ij} = a_{ij}, \quad \bar{\lambda}_{kj} = |c_{kj}| \quad (20)$$

leads to

$$\bar{d}_j^{L,(n)} = \sum_{i=1}^{N_d} \check{c}_i^{(n)} a_{ij} \left(\sum_{l=1}^{N_p} a_{il} \right) \quad (21)$$

and

$$\bar{d}_j^{R,(n)} = \sum_{k=1}^{N_r} \ddot{\psi}_k(0) |c_{kj}| \left(\sum_{l=1}^{N_p} |c_{kl}| \right). \quad (22)$$

This choice is simple to implement, since the (available) standard forward and back projections can be used directly in (21). (Computing $\bar{d}_j^{R,(n)}$ in (22) is negligible compared with (21).) The standard SQS generates a sequence $\{x^{(n)}\}$ in (17) by defining the denominator as

$$\bar{d}_j^{(n)} \triangleq \bar{d}_j^{L,(n)} + \bar{d}_j^{R,(n)}. \quad (23)$$

However, we prefer choices for $\lambda_{ij}^{(n)}$ (and $\lambda_{kj}^{(n)}$) that provide fast convergence. Therefore, we first analyze the convergence rate of the SQS algorithm in terms of the choice of $\lambda_{ij}^{(n)}$ in the next section. Section III introduces acceleration by choosing better $\lambda_{ij}^{(n)}$ (and $\lambda_{kj}^{(n)}$) than the standard choice (20).

D. Convergence Rate of SQS Algorithm

The convergence rate of the sequence $\{x^{(n)}\}$ generated by the SQS iteration (17) depends on the denominator $D^{(n)} \triangleq \text{diag}\{d_j^{(n)}\}$. This paper's main goal is to choose $\lambda_{ij}^{(n)}$ so that the sequence $\{x^{(n)}\}$ converges faster.

The asymptotic convergence rate of a sequence $\{x^{(n)}\}$ that converges to $x^{(\infty)}$ is measured by the root-convergence factor defined as $R_1 \{x^{(n)}\} \triangleq \limsup_{n \rightarrow \infty} \|x^{(n)} - x^{(\infty)}\|^{1/n}$ in [31, p. 288]. The root-convergence factor at $x^{(\infty)}$ for SQS algorithm is given as $R_1 \{x^{(n)}\} = \rho(I - [D^{(\infty)}]^{-1} H^{(\infty)})$ in [31, Linear Convergence Theorem, p. 301] and [42, Theorem 1], where the spectral radius $\rho(\cdot)$ of a square matrix is its largest absolute eigenvalue and $H^{(\infty)} \triangleq \nabla^2 \Psi(x^{(\infty)})$, assuming that $D^{(n)}$ converges to $D^{(\infty)}$. For faster convergence, we want $R_1 \{x^{(n)}\}$ and $\rho(\cdot)$ to be smaller. We can reduce the root-convergence factor based on [42, Lemma 1], by using a smaller denominator $D^{(n)}$ subject to the majorization conditions in (6) and (13).

However, the asymptotic convergence rate does not help us design $D^{(n)}$ in the early iterations, so we consider another factor that relates to the convergence rate of SQS.

Lemma 1: For a fixed denominator D [using the maximum curvature (10)], a sequence $\{x^{(n)}\}$ generated by an SQS algorithm (17) satisfies

$$\Psi(x^{(n+1)}) - \Psi(x^{(\infty)}) \leq \frac{\|x^{(0)} - x^{(\infty)}\|_D^2}{2(n+1)} \quad (24)$$

for any $n \geq 0$, if $\Psi(x)$ is convex. Lemma 1 is a simple generalization of Theorem 3.1 in [39], which was shown for a surrogate with a scaled identity Hessian (using Lipschitz constant). The inequality (24) shows that minimizing $\|x^{(0)} - x^{(\infty)}\|_D^2$ with respect to D will reduce the upper bound of $\Psi(x^{(n)}) - \Psi(x^{(\infty)})$, and thus accelerate convergence. (Since the upper bound is not tight, there should be a room for further acceleration by choosing better D , but we leave it as future work.)

We want to adaptively design $D^{(n)}$ to accelerate convergence at the n th iteration. We can easily extend Lemma 1 to Corollary 1 by treating the current estimate $x^{(n)}$ as an initial image for the next SQS iteration:

Corollary 1: A sequence $\{x^{(n)}\}$ generated by an SQS algorithm (17) satisfies

$$\Psi(x^{(n+1)}) - \Psi(x^{(\infty)}) \leq \frac{\|x^{(n)} - x^{(\infty)}\|_{D^{(n)}}^2}{2} \quad (25)$$

for any $n \geq 0$, if $\Psi(x)$ is convex. The inequality (25) motivates us to use $\|x_j^{(n)} - x_j^{(\infty)}\|$ when selecting $d_j^{(n)}$ (and $\lambda_{ij}^{(n)}$) to accelerate convergence at n th iteration. We discuss this further in Section III-A. We fix $D^{(n)}$ after the n_{fix} number of iterations

²If $D_s^{-1} \succeq D_l^{-1} \succeq H^{(\infty)} \succeq 0$, then $\rho(I - D_s^{-1} H^{(\infty)}) \leq \rho(I - D_l^{-1} H^{(\infty)}) < 1$.

to ensure convergence of SQS iteration (17), based on [20]. In this case, $D^{(n)}$ must be generated by the maximum curvature (10) to guarantee the majorization condition (6) for subsequent iterations.

From (17) and (19), the step size $\Delta_j^{(n)}$ of the SQS iteration (17) has this relationship

$$\Delta_j^{(n)} \triangleq x_j^{(n+1)} - x_j^{(n)} \propto \frac{1}{d_j^{(n)}} \quad (26)$$

where smaller $d_j^{(n)}$ (and relatively larger $\lambda_{ij}^{(n)}$) values lead to larger steps. Therefore, we should encourage $d_j^{(n)}$ to be small ($\lambda_{ij}^{(n)}$ to be relatively large) to accelerate the SQS algorithm. However, we cannot reduce $d_j^{(n)}$ simultaneously for all voxels, due to the majorization conditions in (6) and (13). Lemma 1 (and Corollary 1) suggest intuitively that we should try to encourage larger steps $\Delta_j^{(n)}$ (smaller $d_j^{(n)}$) for the voxels that are far from the optimum to accelerate convergence.

III. SPATIALLY NONUNIFORM SEPARABLE QUADRATIC SURROGATE

We design surrogates that satisfy condition (6) and provide faster convergence based on Section II-D. We introduce the “*update-needed factors*” and propose a spatially nonuniform SQS (NU-SQS) algorithm.

A. Update-Needed Factors

Based on Corollary 1, knowing $|x_j^{(n)} - x_j^{(\infty)}|$ would be helpful for accelerating convergence at the n th iteration, but $x_j^{(\infty)}$ is unavailable in practice. NH-CD algorithm [7] used the difference between the current and previous iteration instead

$$u_j^{(n)} \triangleq \max \left\{ |x_j^{(n)} - x_j^{(n-1)}|, \delta^{(n)} \right\} \quad (27)$$

which we call the “*update-needed factors*” (originally named a voxel selection criterion (VSC) in [7]). Including the small positive values $\{\delta^{(n)}\}$ ensures all voxels to have at least a small amount of attention for updates. This $u_j^{(n)}$ accelerated the NH-CD algorithm by visiting voxels with large $u_j^{(n)}$ more frequently.

B. Design

For SQS, we propose to choose $\lambda_{ij}^{(n)}$ to be larger if the j th voxel is predicted to need more updates based on the “*update-needed factors*” (27) after the n th iteration. We select

$$\tilde{\lambda}_{ij}^{(n)} = a_{ij} u_j^{(n)} \quad (28)$$

which is proportional to $u_j^{(n)}$ and satisfies the condition for $\lambda_{ij}^{(n)}$. This choice leads to the following NU-based denominator:

$$\tilde{d}_j^{L,(n)} = \frac{1}{u_j^{(n)}} \sum_{i=1}^{N_d} \tilde{c}_i^{(n)} a_{ij} \left(\sum_{l=1}^{N_p} a_{il} u_l^{(n)} \right) \quad (29)$$

which leads to spatially nonuniform updates $\Delta_j^{(n)} \propto u_j^{(n)}$.

If it happened that

$$|x_j^{(n)} - x_j^{(\infty)}| \approx B |x_j^{(n)} - x_j^{(n-1)}| \text{ for all } j \quad (30)$$

where B is a constant, then the NU denominator $\tilde{d}_j^{L,(n)}$ would minimize the upper bound of $\Psi(x^{(n+1)}) - \Psi(x^{(\infty)})$ in Corollary 1:

Lemma 2: The proposed choice $\tilde{d}_j^{L,(n)}$ in (29) minimizes the following weighted sum of the denominators:

$$\sum_{j=1}^{N_p} \left(u_j^{(n)} \right)^2 d_j^{L,(n)} \quad (31)$$

over all possible choices of the $d_j^{L,(n)}$ in (19).

Proof: In Appendix A. ■

The proposed $\tilde{d}_j^{L,(n)}$ in (29) reduces to the standard choice $\bar{d}_j^{L,(n)}$ in (21) when $\{u_j^{(n)}\}$ is uniform. Similar to the standard choice $\bar{d}_j^{L,(n)}$, the proposed choice $\tilde{d}_j^{L,(n)}$ can be implemented easily using standard forward and back projection. However, since $\tilde{d}_j^{L,(n)}$ depends on iteration (n), additional projections required for $\tilde{d}_j^{L,(n)}$ at every iteration would increase computation. We discuss ways to reduce this burden in Section III-F.

Similar to the data-fit term, we derive the denominator of NU-SQS for the regularizer term to be

$$\tilde{d}_j^{R,(n)} = \frac{1}{u_j^{(n)}} \sum_{k=1}^{N_r} \tilde{\psi}_k(0) |c_{kj}| \left(\sum_{l=1}^{N_p} |c_{kl}| u_l^{(n)} \right) \quad (32)$$

from the choice $\tilde{\lambda}_{kj}^{(n)} = |c_{kj}| u_j^{(n)}$ and the maximum curvature method in [14]. Alternatively, we may use Huber’s optimal curvature [32, Lemma 8.3, p.184] replacing $\tilde{\psi}_k(0)$ in (32) by $\tilde{\psi}_k([Cx^{(n)}]_k)/[Cx^{(n)}]_k$. The computation of (32) is much less than that of the data-fit term.

Defining the denominator in the SQS iteration (17) as

$$\tilde{d}_j^{(n)} \triangleq \tilde{d}_j^{L,(n)} + \tilde{d}_j^{R,(n)} \quad (33)$$

leads to the accelerated NU-SQS iteration, while the algorithm monotonically decreases $\Psi(x)$ and is provably convergent [20]. We can further accelerate NU-SQS by OS methods [13], [14], while losing the guarantee of monotonicity. This algorithm, called OS algorithms based on a spatially nonuniform SQS (NU-OS-SQS), is explained in Section IV.

C. Dynamic Range Adjustment of $u_j^{(n)}$

In reality, (30) will not hold, so (27) will be suboptimal. We could try to improve (27) by finding a function $f^{(n)}(\cdot) : [\delta^{(n)}, \infty) \rightarrow [\epsilon, 1]$ based on the following:

$$\arg \min_{f^{(n)}(\cdot)} \sum_{j=1}^{N_p} \left(f^{(n)}(u_j^{(n)}) - \frac{|x_j^{(n)} - x_j^{(\infty)}|}{\max_l |x_l^{(n)} - x_l^{(\infty)}|} \right)^2 \quad (34)$$

where ϵ is a small positive value. Then we could use $f^{(n)}(u_j^{(n)})$ as (better) update-needed factors. However, solving (34) is in-

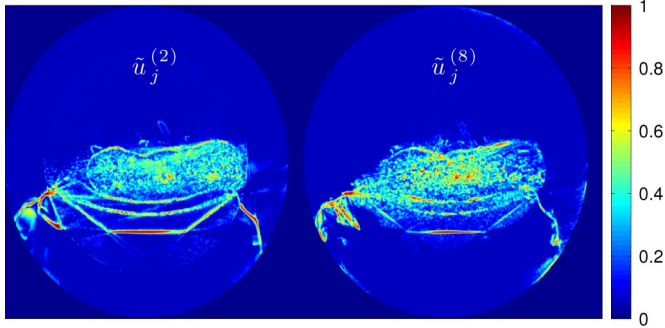


Fig. 2. Shoulder region scan: $\tilde{u}_j^{(2)}$ and $\tilde{u}_j^{(8)}$ after DRA for NU-OS-SQS(82 subsets), with the choice $g(v) = \max\{v^{1b}, 0.05\}$. NU-OS-SQS updates the voxels with large $\tilde{u}_j^{(n)}$ more, whereas ordinary OS-SQS updates all voxels equivalently.

tractable, so we searched empirically for good candidates for a function $f^{(n)}(\cdot)$.

Intuitively, if the dynamic range of the update-needed factors $u_j^{(n)}$ in (27) is too wide, then there will be too much focus on the voxels with relatively large $u_j^{(n)}$, slowing the overall convergence rate. On the other hand, a narrow dynamic range of $u_j^{(n)}$ will provide no speed-up, since the algorithm will distribute its efforts uniformly. Therefore, adjusting the dynamic range of the update-needed factors is important to achieve fast convergence. This intuition corresponds to how the NH-CD approach balanced between homogeneous update orders and nonhomogeneous update orders [7].

To adjust the dynamic range and distribution of $u_j^{(n)}$, we first construct their empirical cumulative density function

$$F_{\text{cdf}}^{(n)}(u) \triangleq \frac{1}{N_p} \sum_{j=1}^{N_p} I_{\{u_j^{(n)} \leq u\}} \quad (35)$$

to somewhat normalize their distribution, where $I_B = 1$ if B is true or 0 otherwise. Then we map the values of $F_{\text{cdf}}^{(n)}(u)$ by a nondecreasing function $g(\cdot) : [0, 1] \rightarrow [\epsilon, 1]$ as follows:

$$\tilde{u}_j^{(n)} \triangleq f^{(n)}(u_j^{(n)}) = g\left(F_{\text{cdf}}^{(n)}(u_j^{(n)})\right) \quad (36)$$

which controls the dynamic range and distribution of $\{u_j^{(n)}\}_{j=1}^{N_p}$, and we enforce positivity in $g(\cdot)$ to ensure that the new adjusted parameter $\tilde{\lambda}_{ij}^{(n)} = a_{ij}\tilde{u}_j^{(n)}$ is positive if a_{ij} is positive. (We set $\delta^{(n)}$ in (27) to zero here, since a positive parameter ϵ ensures the positivity of $\tilde{\lambda}_{ij}^{(n)}$ if a_{ij} is positive.) The transformation (36) from $u_j^{(n)}$ to $\tilde{u}_j^{(n)}$ is called dynamic range adjustment (DRA), and two examples of such $\tilde{u}_j^{(n)}$ are presented in Fig. 2. Then we use $\tilde{u}_j^{(n)}$ instead of $u_j^{(n)}$ in (28).

Here, we focus on the following function for adjusting the dynamic range and distribution:

$$g(v) \triangleq \max\{v^t, \epsilon\} \quad (37)$$

where t is a nonnegative real number that controls the distribution of $\tilde{u}_j^{(n)}$ and ϵ is a small positive value that controls the maximum dynamic range of $\tilde{u}_j^{(n)}$. The function reduces to the ordinary SQS choice in (20) when $t = 0$. The choice of $g(\cdot)$,

particularly the parameters t and ϵ here, may influence the convergence rate of NU-SQS for different data sets, but we show that certain values for t and ϵ consistently provide fast convergence for various data sets.

D. Related Work

In addition to the standard choice (20), the choice

$$\lambda_{ij}^{(n)} = a_{ij} \max\{x_j^{(n)}, \delta\} \quad (38)$$

with a small nonnegative δ , has been used in emission tomography problems [35], [36] and in transmission tomography problems [11], [37]. This choice is proportional to $x_j^{(n)}$, and thereby provides a relationship $\Delta_j^{(n)} \propto x_j^{(n)}$. This classical choice (38) can be also viewed as another NU-SQS algorithm based on ‘‘intensity.’’ However, intensity is not a good predictor of which voxels need more update, so (38) does not provide fast convergence based on the analysis in Section II-D.

E. Initialization of $u_j^{(0)}$

Unfortunately, $u_j^{(n)}$ in (27) is available only for $n \geq 1$, i.e., after updating all voxels once. To define the initial update factors $u_j^{(0)}$, we apply edge and intensity detectors to an initial filtered back-projection (FBP) image. This is reasonable since the initial FBP image is a good low-frequency estimate, so the difference between initial and final image will usually be larger near edges. We investigated one particular linear combination of edge and intensity information from an initial image. We used the 2-D Sobel operator to approximate the magnitude of the gradient of the image within each transaxial plane. Then we scaled both the magnitude of the approximated gradient and the intensity of the initial image to have same maximum value, and computed a linear combination of two arrays with a ratio 2 : 1 for the initial update-needed factor $u_j^{(0)}$, followed by DRA method. We have tried other linear combinations with different ratios, but the ratio 2 : 1 provided the fastest convergence rate in our experiments.

F. Implementation

The dependence of $\lambda_{ij}^{(n)}$ on iteration (n) increases computation, but we found two practical ways to reduce the burden. First, we found that it suffices to update $\tilde{u}_j^{(n)}$ (and $\tilde{d}_j^{(n)}$) every $n_{\text{loop}} > 1$ iterations instead of every iteration. This is reasonable since the update-needed factors usually change slowly with iteration. In this case, we must generate a surrogate with the maximum curvature (10) to guarantee the majorization condition (6) for all iterations. Second, we compute the NU-based denominator (29) simultaneously with the data-fit gradient in (17). In 3-D CT, we use forward and back-projectors that compute elements of the system matrix A on the fly, and those elements are used for the gradient $\nabla L(x)$ in (17). For efficiency, we reuse those computed elements of A for the NU-based denominator (29). We implemented this using modified separable footprint projector subroutines [43] that take two inputs and project (or back-project) both. This approach required only 29% more computation time than a single forward projection rather than doubling the time (see Table I). Combining this approach with $n_{\text{loop}} = 3$ yields a NU-SQS algorithm that required only 11%

TABLE I
 RUN TIME OF ONE ITERATION OF NU-OS-SQS (82 SUBSETS) FOR
 DIFFERENT CHOICE OF n_{loop} FOR GE PERFORMANCE PHANTOM

	SQS	OS-SQS(82)	NU-OS-SQS(82)		
n_{loop}	·	·	1	3	5
1 Iter. [sec]	82	125	161	139	133

more computation time per iteration than standard SQS, but converges faster.

Computing $\tilde{u}_j^{(n)}$ and the corresponding NU-based denominator requires one iteration each. In the proposed algorithm, we computed $\tilde{u}_j^{(n)}$ during one iteration, and then computed the NU-based denominator (29) during the next iteration combined with the gradient computation $\nabla L(x)$. Then we used the denominator for n_{loop} iterations and then compute $\tilde{u}_j^{(n)}$ again to loop the process (see outline in Appendix B).

IV. IMPROVED ORDERED SUBSETS ALGORITHM FOR HELICAL CT

OS methods can accelerate algorithms by a factor of the number of subsets in early iterations, by using a subset of the measured data for each subset update. However, in practice, OS methods break the monotonicity of SQS and NU-SQS, and typically approach a limit-cycle looping around the optimum. This section describes a simple idea that reduces this problem, only slightly affecting the convergence rate unlike previous convergent OS algorithms. In helical CT geometries, we observed that conventional OS algorithms for PL and PWLS problem are unstable for large subset numbers as they did not consider their nonuniform sampling. Thus, we describe an improved OS algorithm that is more stable for helical CT.

A. Ordinary OS Algorithm

An OS algorithm (with M subsets) for accelerating the SQS or NU-SQS updates (17) has the following m th sub-iteration within the n th iteration using the denominator³ $\tilde{d}_j^{(n)}$ in (33)

$$x_j^{(n+(m+1)/M)} = \left[x_j^{(n+m/M)} - \frac{1}{\tilde{d}_j^{(n)}} \left(\hat{\gamma}_j^{(n+m/M)} \frac{\partial}{\partial x_j} L_m(x^{(n+m/M)}) + \frac{\partial}{\partial x_j} R(x^{(n+m/M)}) \right) \right]_+ \quad (39)$$

where $\hat{\gamma}_j^{(n+m/M)}$ scales the gradient of a subset data-fit term $L_m(x) = \sum_{i \in S_m} h_i([Ax]_i)$, and S_m consists of projection views in m th subset for $m = 0, 1, \dots, M-1$. We count one iteration when all M subsets are used once, since the projection A used for computing data-fit gradients is the dominant operation in SQS iteration.

If we use many subsets to attempt a big acceleration in OS algorithm, some issues arise. The increased computation for the gradient of regularizer in (39) can become a bottleneck (this has

³We consider the maximum curvature (10) here for computational efficiency in OS methods.

been relieved in [44]). Also having less measured data in each subset will likely break the subset balance condition

$$\nabla L_0(x) \approx \nabla L_1(x) \approx \dots \approx \nabla L_{M-1}(x). \quad (40)$$

The update in (39) would accelerate the SQS algorithm by exactly M if the scaling factor $\hat{\gamma}_j^{(n+m/M)}$ satisfied the condition

$$\hat{\gamma}_j^{(n+m/M)} = \frac{\frac{\partial}{\partial x_j} L(x^{(n+m/M)})}{\frac{\partial}{\partial x_j} L_m(x^{(n+m/M)})}. \quad (41)$$

It would be impractical to compute this factor exactly, so the conventional OS approach is to simply use the constant $\gamma = M$. This ‘‘approximation’’ often works well in the early iterations when the subsets are suitably balanced, and for small number of subsets. But in general, the errors caused by the differences between $\hat{\gamma}_j^{(n+m/M)}$ and a constant scaling factor γ cause two problems in OS methods. First, the choice $\gamma = M$ causes instability in OS methods in a helical CT that has limited projection views outside ROI, leading to very imbalanced subsets. Therefore, we propose an alternative choice γ_j that better stabilizes OS for helical CT in Section IV-B. Second, even with γ replaced by γ_j , OS methods approach a limit-cycle that loops around the optimal point within sub-iterations [25]. Section IV-C considers a simple averaging idea that reduces this problem.

B. Proposed OS Algorithm in Helical CT

The constant scaling factor $\gamma = M$ used in the ordinary regularized OS algorithm is reasonable when all the voxels are sampled uniformly by the projection views in all the subsets. But in geometries like helical CT, the voxels are nonuniformly sampled. In particular, voxels outside the ROI are sampled by fewer projection views than voxels within the ROI (see Fig. 1). So some subsets make no contribution to such voxels, i.e., very imbalanced subsets. We propose to use a voxel-based scaling factor γ_j that considers the nonuniform sampling, rather than a constant factor γ .

After investigating several candidates, we focused on the following scaling factor:

$$\gamma_j = \sum_{m=0}^{M-1} I_{\left\{ \sum_{i \in S_m} \tilde{c}_i^{(n)} a_{ij} \left(\sum_{l=1}^{N_p} a_{il} \tilde{u}_l^{(0)} \right) > 0 \right\}} \quad (42)$$

where $I_B = 1$ if B is true or 0 otherwise. As expected, $\gamma_j < M$ for voxels outside the ROI and $\gamma_j = M$ for voxels within the ROI. The scaling factor (42) has small compute overhead as it can be computed simultaneously with the precomputation of the initial data-fit denominator (29) by rewriting it as

$$\tilde{d}_j^{L,(0)} \triangleq \frac{1}{\tilde{u}_j^{(0)}} \sum_{m=0}^{M-1} \left(\sum_{i \in S_m} \tilde{c}_i^{(n)} a_{ij} \left(\sum_{l=1}^{N_p} a_{il} \tilde{u}_l^{(0)} \right) \right). \quad (43)$$

We store (42) as a short integer for each voxel outside the ROI only, so it does not require very much memory.

We evaluated the OS algorithm with the proposed scaling factors (42) using the GE performance phantom. Fig. 3 shows that the OS algorithm using the proposed scaling factors (42) leads to more stable reconstruction than the ordinary OS approach which diverges outside the ROI. The instability seen with the ordinary

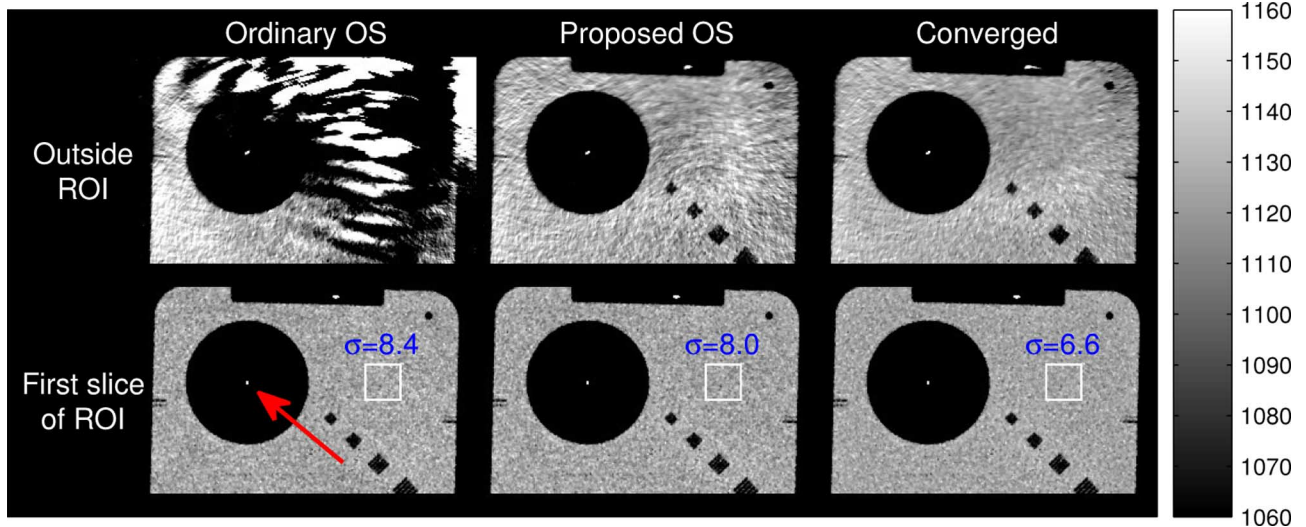


Fig. 3. Effect of gradient scaling in regularized OS-SQS algorithm with GE performance phantom in helical CT: Each image is reconstructed after running 20 iterations of OS algorithm with 328 subsets, using ordinary and proposed scaling approaches. Standard deviation σ of a uniform region (in white box) is computed for comparison. We compute FWHM of a tungsten wire (red arrow) to measure the resolution. (The result of a convergent algorithm is shown for reference. Images are cropped for better visualization).

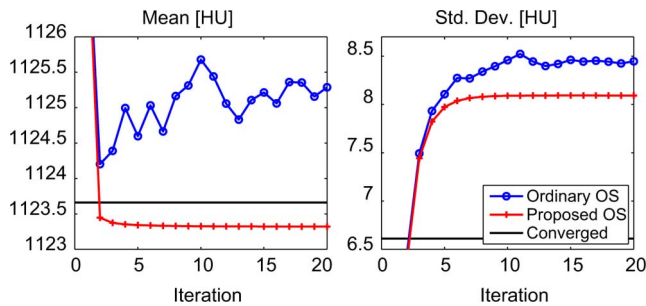


Fig. 4. GE performance phantom: mean and standard deviation within a uniform region in the first slice of the ROI (see Fig. 3) versus iteration, showing the instability of ordinary OS approach with 328 subsets, compared with the proposed OS approach. Also shown is the result from a converged image $x^{(\infty)}$ generated from several iterations of a convergent algorithm.

OS approach may also degrade image quality within the ROI as seen by the noise standard deviations in Fig. 3. The results in Fig. 4 further show that the ordinary OS algorithm exhibits more variations within the ROI due to the instability outside ROI, whereas the proposed OS algorithm is robust.

C. OS Algorithm With Averaging

Although the new scaling factors (42) stabilize OS in helical CT and reduce artifacts, the final noise level is still worse than a convergent algorithm (see Figs. 3 and 4) because any OS method with constant scaling factors will not converge [45]. This section discusses one practical method that can reduce noise without affecting the convergence rate. This approach helps the OS algorithm come closer to the converged image, reducing the undesirable noise in images reconstructed using OS algorithms with large M .

To ensure convergence, the incremental optimization transfer method [26] was proposed, which involves a form of averaging, but the greatly increased memory space required has prevented its application in 3-D X-ray CT. As a practical alternative, we

TABLE II
GE PERFORMANCE PHANTOM: NOISE, RESOLUTION AND RMSD BEHAVIOR OF OS-SQS(328 SUBSETS) AFTER 20 ITERATIONS FOLLOWED BY AVERAGING

	Smoothed FBP	OS-SQS(328)		Conv.
		w/o averaging	w/ averaging	
Mean [HU]	1127.7	1123.3	1123.8	1123.7
Std. Dev. [HU]	2.3	8.0	7.2	6.6
FWHM [mm]	1.4	0.7	0.7	0.7
RMSD [HU]	9.4	3.4	0.8	.

investigated an approach where the final image is formed by averaging all of the sub-iterations at the final iteration n_{end} of the OS algorithm (after it approaches its limit cycle). A memory-efficient implementation of this approach uses a recursive in-place calculation

$$\bar{x}^{((m+1)/M)} = \frac{m}{m+1} \bar{x}^{(m/M)} + \frac{1}{m+1} x^{(n_{\text{end}}-1+(m+1)/M)} \quad (44)$$

where $\bar{x}^{(0)}$ is an initial zero image, and $\bar{x}^{(1)}$ is the final averaged image. There was a preliminary simulation investigation of averaging the final iteration in [27], and we applied the averaging technique to CT scans here. In Table II, we investigated this averaging method using a scan of the GE performance phantom (GEPP) phantom and quantified the noise and resolution properties (as described in Fig. 3), and evaluated root mean square difference (RMSD⁴) between current and converged image within ROI. Table II shows that the averaging technique successfully reduces the noise and RMSD.

Overall, we have enhanced the standard OS-SQS algorithm into the NU-OS-SQS method for 3-D helical CT. First, we accelerated the standard OS-SQS algorithm by nonuniform (NU) approach, encouraging larger step sizes for the voxels that need more updates. We modified the algorithm to handle the helical

⁴RMSD $\triangleq \left\| x_{\text{ROI}}^{(n)} - x_{\text{ROI}}^{(\infty)} \right\|_2 / \sqrt{N_{p,\text{ROI}}}$ [HU], where $N_{p,\text{ROI}}$ is the number of voxels in the ROI.

CT geometry by introducing the scaling factor γ_j . We also averaged all sub-iterations at the final iteration to reduce noise. The outline of the proposed algorithm is presented in Appendix B. We investigate the performance of the NU-OS-SQS algorithm for various CT scans in the next section.

V. EXPERIMENTAL RESULTS

We investigated the proposed NU-OS-SQS algorithm for PWLS image reconstruction with a nonnegativity constraint. The PWLS cost function is strictly convex and has a unique global minimizer [46]. We implemented the NU-OS-SQS algorithm in C and executed it on a Mac with two 2.26 GHz quad-core Intel Xeon processors and a 16 GB RAM. We used 16 threads, and projection views were grouped and assigned to each thread.

Three 3-D helical CT data sets are used in this section to compare the proposed NU-OS-SQS algorithm to the ordinary OS-SQS algorithm, and we used the GEPP to measure the resolution. We used two other clinical data sets to investigate the performance of NU approach. We investigated tuning the DRA function $g(\cdot)$ in (37) to provide fast convergence rate for various data sets. We also provide results from a simulation data set in a supplementary material for reproducibility.⁵

We chose the parameters of the cost function $\Psi(x)$ in (2) to provide a good image. We defined an edge-preserving potential function as $\psi_k([Cx]_k) \triangleq \bar{\omega}_k \psi([Cx]_k)$, where the function:⁶

$$\psi(t) = \frac{\delta^2}{b^3} \left(\frac{ab^2}{2} \left| \frac{t}{\delta} \right|^2 + b(b-a) \left| \frac{t}{\delta} \right| + (a-b) \log \left(1 + b \left| \frac{t}{\delta} \right| \right) \right) \quad (45)$$

is a generalized version of a Fair potential function in [47], and the spatial weighting $\bar{\omega}_k$ [48] provides resolution properties that emulate the GE product “Veo.” We used $M = 82$ subsets for the OS algorithms, assigning 12 out of 984 projection views per rotation to each subset. We used the maximum curvature (10) for generating the denominator of surrogate function of the cost function $\Psi(x)$, and focused on $n_{\text{loop}} = 3$ which balances the convergence rate and run time, based on Table I.

In Section II-D, we recommended fixing the denominator $\tilde{d}_j^{(n)}$ [generated by the maximum curvature (10)] after n_{fix} iterations in NU-SQS algorithm to guarantee convergence. This condition is less important theoretically when we accelerate the NU-SQS algorithm with OS methods that break the convergence property. However, we still recommend fixing $\tilde{d}_j^{(n)}$ after n_{fix} iterations (before approaching the limit-cycle) in the NU-OS-SQS algorithm, because we observed some instability from updating $\tilde{d}_j^{(n)}$ (and $\tilde{u}_j^{(n)}$) every n_{loop} iterations near the limit-cycle in our experiments. We selected $n_{\text{fix}} = 7$ for GEPP, but we did not use n_{fix} for other two cases because the algorithm did not reach a limit-cycle within $n_{\text{end}} = 20$ iterations, and we leave optimizing n_{fix} as a future work.

⁵The supplementary material is available at <http://ieeexplore.ieee.org>.

⁶The gradient $\psi'(t) = t(1 + a|t/\delta|)/(1 + b|t/\delta|)$ avoids expensive power operations, saving computation for OS-type methods. The function reduces to a Fair potential function in [47] when $a = 0$ and $b = 1$. We used $a = 0.0558$, $b = 1.6395$, and $\delta = 10$ in our experiments.

In Section IV-B, we stabilized the OS-SQS algorithm outside ROI in helical geometry by using the factor γ_j in (42). However, we experienced some instability outside ROI in NU-OS-SQS methods even with (42), because a small NU denominator $\tilde{d}_j^{(n)}$ outside ROI is more likely to lead to instability than for voxels within the ROI due to the incomplete sampling outside ROI. Therefore, we prevent the denominator $\tilde{d}_j^{(n)}$ outside ROI from being very small. We empirically modified the DRA function in Section III-C, and used it for our experiments, improving stability outside ROI. We first modified the function (35) as follows:

$$F_{\text{cdf}}^{(n)}(u) \triangleq \frac{1}{N_p} \sum_{j=1}^{N_p} I_{\{\gamma_j u_j^{(n)} \leq u\}} \quad (46)$$

since the value of $u_j^{(n)}$ in (27) outside ROI was found to be relatively large due to the incomplete sampling. We further modified (36) and (37) to prevent $\tilde{d}_j^{(n)}$ from becoming very small outside ROI as follows with $g(v; \alpha) \triangleq \max\{\alpha v^t, \epsilon\}$:

$$\tilde{u}_j^{(n)} \triangleq \begin{cases} g\left(F_{\text{cdf}}^{(n)}(\gamma_j u_j^{(n)}); 1\right), & \text{if } j\text{th voxel within ROI} \\ g\left(F_{\text{cdf}}^{(n)}(\gamma_j u_j^{(n)}); 0.5\right), & \text{otherwise.} \end{cases} \quad (47)$$

A. GE Performance Phantom

We reconstructed $512 \times 512 \times 47$ images of the GEPP from a $888 \times 64 \times 3071$ sinogram (the number of detector columns \times detector rows \times projection views) with pitch 0.5. We evaluated the full-width at half-maximum (FWHM) of a tungsten wire (see Fig. 3). Fig. 5(a) shows the resolution versus run time and confirms that nonuniform (NU) approach accelerates the SQS algorithm. This dramatic speed-up in FWHM is promising since SQS-type algorithms are known to have slow convergence rate of high frequency components [6]. We also evaluated the convergence rate by computing RMSD between current and converged⁷ image versus run time, within ROI.

Fig. 5(a) and (b) illustrates that increasing t in $g(\cdot)$ in (37) accelerates the convergence of “update-needed” region, particularly the wire and edges in GEPP. However, highly focusing the updates on few voxels will not help speed up the overall convergence for all objects. Therefore, we further investigate the choice of $g(\cdot)$ using various patient CT scans.

The RMSD plots⁸ of NU-OS-SQS in Fig. 5(b) reached a limit-cycle after 1500 s that did not approach zero. Averaging the sub-iterations at the final iteration improved the final image with small computation cost, yielding the drop in RMSD at the last 20th iteration in Fig. 5(b). The reduced noise was measurable in the reconstructed image, as seen in Table II.

B. Shoulder Region Scan

In this experiment, we reconstructed a $512 \times 512 \times 109$ image from a shoulder region scan $888 \times 32 \times 7146$ sinogram with pitch

⁷We ran 100 iterations of OS-SQS algorithm with 41 subsets, followed by each 100 iterations of OS-SQS algorithm with four subsets, and 2000 iterations of (convergent) SQS. We subsequently performed 100 iterations of (convergent) NH-ABCD-SQS [21] to generate (almost) converged images $x^{(\infty)}$.

⁸We also provide the plots of the cost function for GEPP and shoulder region scan in the supplementary material.

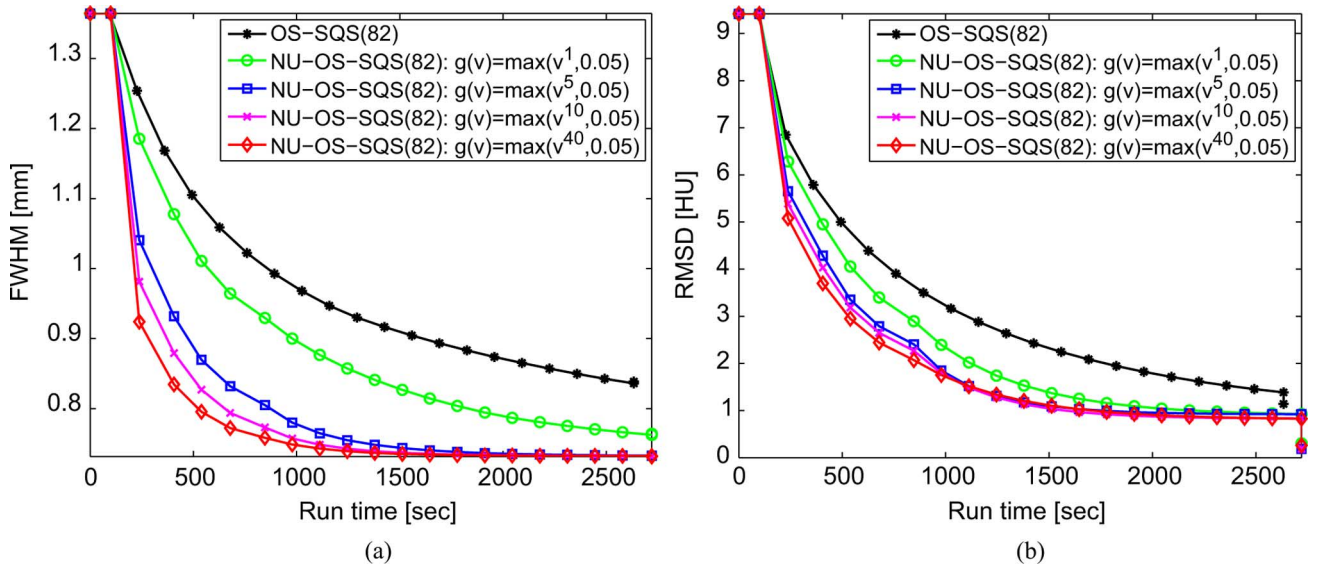


Fig. 5. GE performance phantom: plots of (a) FWHM and (b) RMSD as a function of run time for different choice of DRA parameters t for $\epsilon = 0.05$. Plot markers show each iteration. There are no changes during first iteration, since we consider precomputing the denominator using one forward and back projections as one iteration.

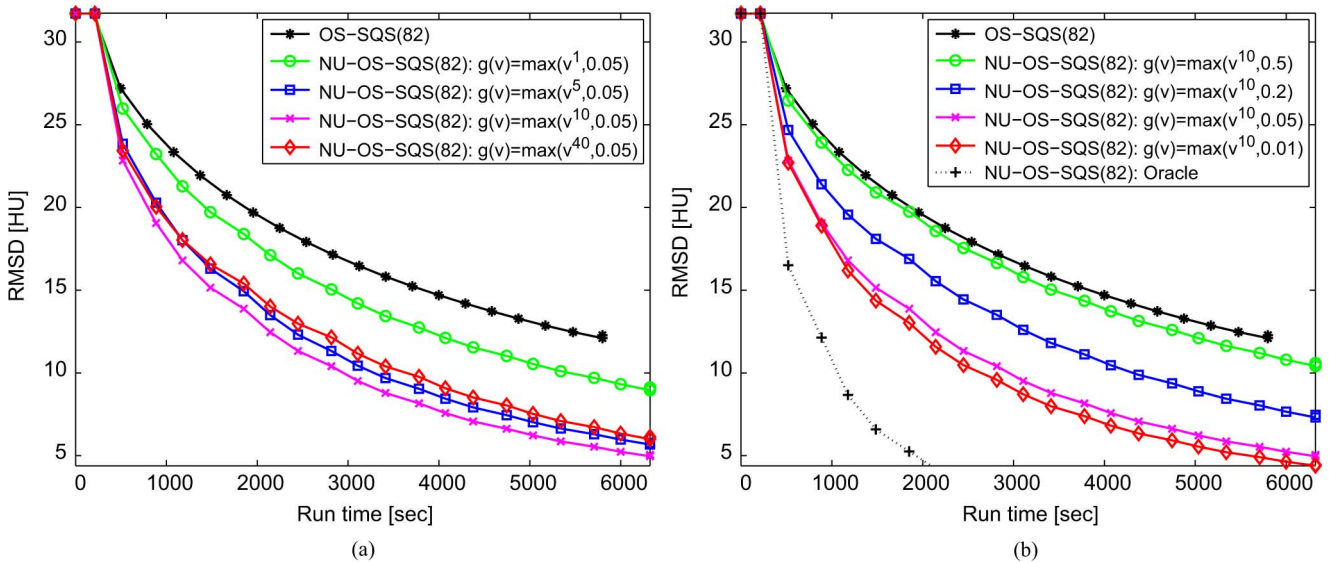


Fig. 6. Shoulder region scan: plot of RMSD versus run time for different choice of parameters (a) t and (b) ϵ in $g(v) = \max\{v^t, \epsilon\}$.

0.5. Fig. 6(a) and (b) shows that the nonuniform approach accelerates convergence, depending on the choice of parameters in $g(\cdot)$. We investigated the relationship between the convergence rate and the DRA function $g(\cdot)$ by tuning both the parameters t and ϵ in (37). Fig. 6(a) shows that increasing t to 10 accelerated convergence, but larger t values did not help as the choice of $t = 40$ was slower than $t = 10$. In Fig. 6(b), decreasing ϵ to 0.01 accelerated the algorithm in this shoulder region scan, but not for the data set in Section V-C, so $\epsilon = 0.05$ appears to be a reasonable choice overall.

We averaged the sub-iterations at the last iteration, but Fig. 6(a) and (b) did not show a drop at the final iteration [which appeared in Fig. 5(b)], because the algorithm had not yet reached a limit-cycle. Even though averaging did not noticeably decrease the RMSD, the reconstructed image had measurable noise reduction in regions that already reached a limit-cycle like uniform regions. (Results not shown.)

In Fig. 7(a), we illustrate that statistical image reconstruction can reduce noise and preserve image features compared to analytical FBP reconstruction. The reconstructed images of (NU-)OS-SQS show that NU approach helps OS-SQS to approach the converged image faster than the ordinary method. After the same computation (95 min), the reconstructed image of OS-SQS still contains streaks from the initial FBP image, while NU-OS-SQS has reduced the streaks. This is apparent in the difference images between the reconstructed and converged images in Fig. 7(b).

By analyzing NU-OS-SQS in two CT scans, we observed that the parameters $t = 10$ and $\epsilon = 0.05$ consistently accelerated the algorithm by about a factor of more than two.⁹ (The choice

⁹We used the run time and RMSD of standard OS-SQS after 20 iterations (without averaging) as a reference to compare with the NU-OS-SQS for each data set. Then we compared the run time of NU-OS-SQS that is required for achieving the reference RMSD with the reference run time, and confirmed that NU provided more than two-fold accelerations in two CT scans.

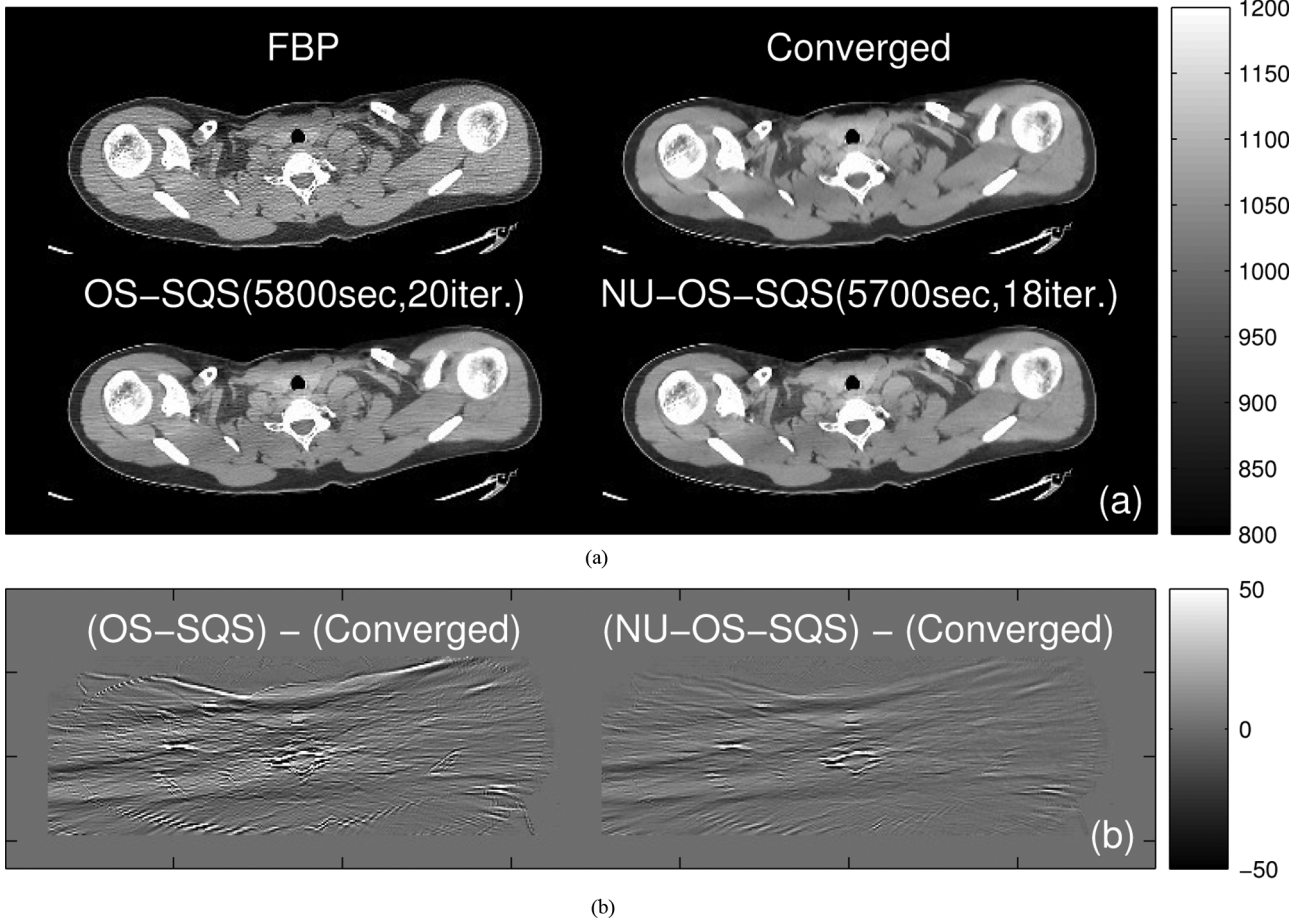


Fig. 7. Shoulder region scan. (a) Center slice of initial FBP, converged image and reconstructed image by OS-SQS(82) and NU-OS-SQS(82)- $g(v) = \max\{v^{10}, 0.05\}$ after about 95 min. (b) Difference between the reconstructed and converged images are additionally shown to illustrate the acceleration of NU approach. (Images are cropped for better visualization).

$\epsilon = 0.01$ was too aggressive in our other experiments.) We also have observed more than two-fold accelerations in other experiments. (Results not shown.) Fig. 6(b) shows the RMSD plot using the (practically unavailable) oracle update-needed factor $\hat{u}_j^{(n)} \triangleq |x_j^{(n)} - x_j^{(\infty)}|$ instead of our heuristic choice $\tilde{u}_j^{(n)}$. This result suggests that additional optimization of the DRA method and initialization of $\tilde{u}_j^{(0)}$ could further speed up the NU algorithm in future work.

C. Truncated Abdomen Scan

We also reconstructed a $390 \times 390 \times 239$ image from a $888 \times 64 \times 3516$ sinogram with pitch 1.0. This scan contains transaxial truncation and the initial FBP image has truncation artifacts [49] that can be reduced by iterative reconstruction. The choice of $u_j^{(0)}$ described in Section III-E did not consider truncation effects, and we found that NU-OS-SQS did not reduce such artifacts faster than standard OS-SQS. (The large patient size may also have reduced the possible speed-up by the NU method, compared to the previous two scans.) Therefore, we investigated an alternative NU method that can reduce truncation artifacts faster than standard algorithm.

We designed a modified NU method using a few (m_{sub}) sub-iterations of standard OS-SQS to generate the initial update-needed factor $u_j^{(0)}$, which may also be a reasonable approach for other scans. We perform initial sub-iterations $x_{\text{sub}}^{(m/M)}$ in (39)

efficiently using two-input projectors (in Section III-F) and replacing the all-view denominator $\tilde{d}_j^{L,(n)}$ in (29) by a standard subset-based denominator [25]

$$\tilde{d}_{j,\text{sub}}^{L,m,(m/M)} \triangleq \gamma \sum_{i \in S_m} \tilde{c}_i^{(m/M)} a_{ij} \left(\sum_{l=1}^{N_p} a_{il} \right) \quad (48)$$

where S_m consists of projection views in m th subset. The scaling factor γ_j in (42) is unavailable at this point, so we use $\gamma = M$ instead. After m_{sub} sub-iterations, we compute the following initial update-needed factors:

$$\tilde{u}_j^{(0)} \triangleq f_{\text{sub}}^{(m_{\text{sub}}/M)} \left(\left| x_{j,\text{sub}}^{(m_{\text{sub}}/M)} - x_j^{(0)} \right| \right) \quad (49)$$

where $f_{\text{sub}}^{(m_{\text{sub}}/M)}(\cdot)$ is a DRA function in (36), and we use these to compute the NU denominators $\tilde{d}_j^{L,(0)}$ and $\tilde{d}_j^{R,(0)}$ that we use for first n_{loop} outer iterations.

Fig. 8(a) shows that statistical image reconstruction provides better image quality than FBP reconstruction. Fig. 8(b) illustrates that this NUsub-OS-SQS approach reduces the truncation artifacts faster than the standard OS-SQS and NU-OS-SQS. Although standard OS-SQS reduces noise faster than other two algorithms in Fig. 8(b), both NU-OS-SQS and NUsub-OS-SQS show better convergence near the spine, the boundary of patient, and other internal structures than OS-SQS at the same computation time (90 min).

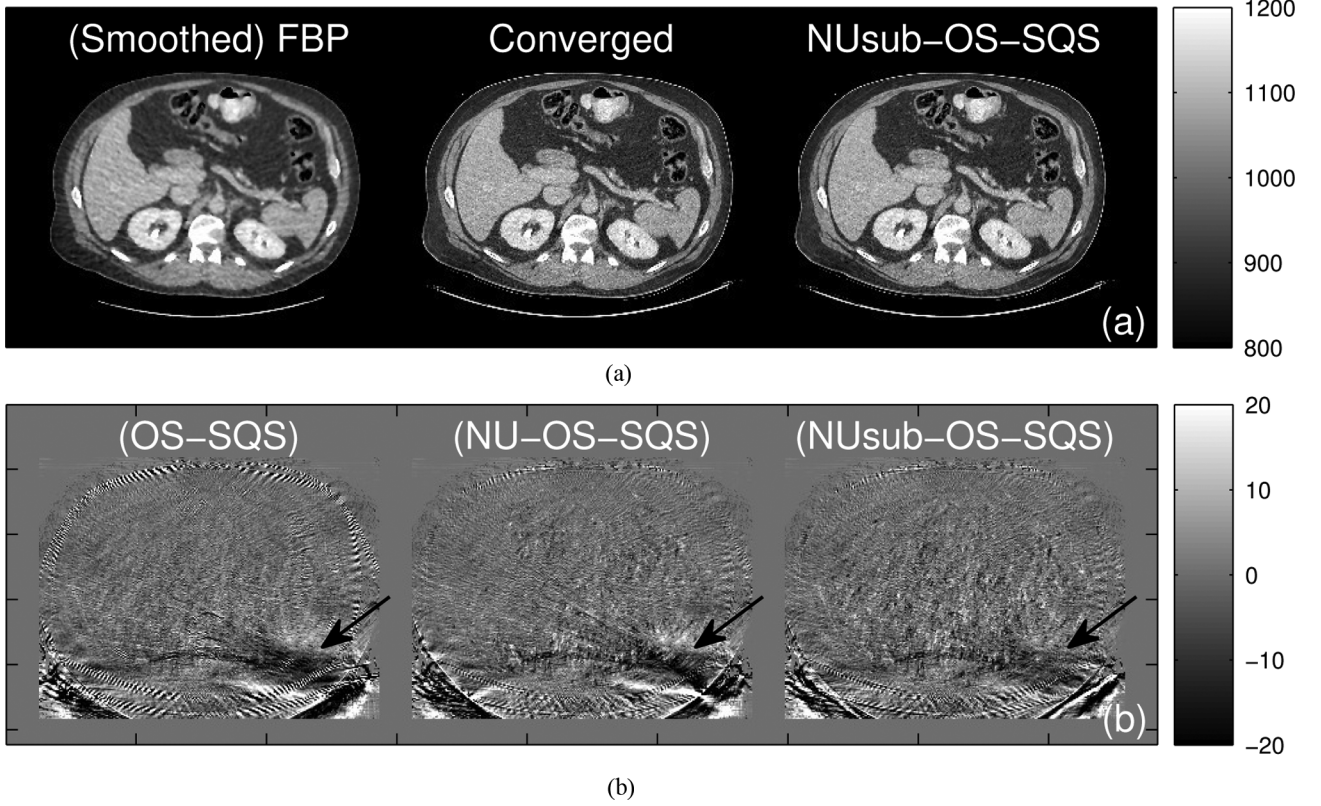


Fig. 8. Truncated abdomen scan. (a) Center slice of FBP, converged image, and reconstructed image by NUsub-OS-SQS(82)- $g(v) = \max\{v^{10}, 0.05\}$ using $\tilde{u}_j^{(0)}$ in (49) generated from sub-iterations. (b) Difference between the reconstructed and converged images, where images are reconstructed by OS-SQS(82) after 5400 s (20 iterations), NU-OS-SQS(82) after 5230 s (18 iterations) using $\tilde{u}_j^{(0)}$ extracted from FBP based on Section III-E, and NUsub-OS-SQS(82) after 5220 s (17 iterations) using $\tilde{u}_j^{(0)}$ in (49). The (black) arrows indicate truncation artifacts. Images are cropped for better visualization.

VI. CONCLUSION

This paper has presented a spatially nonuniform SQS algorithm that can efficiently minimize both PL and PWLS problems monotonically. The experimental results show that the proposed NU-SQS approach converged more than twice as fast as SQS. The OS algorithm, further applied to SQS method for acceleration, was enhanced to handle nonuniformly sampled geometries such as helical CT. The improvements showed promising results on large 3-D helical CT data sets.

The key of the NU-SQS approach is designing “update-needed” factors $u_j^{(n)}$ in (27) that encourage larger step sizes for voxels that are predicted to need larger changes to reach the final image. Further optimization of these factors, e.g., by improving the initialization of $\tilde{u}_j^{(0)}$ and the DRA function in (36), should lead to further acceleration and stability of the proposed NU-SQS and NU-OS-SQS methods.

APPENDIX A PROOF OF LEMMA 2

The proposed choice $\tilde{\lambda}_{ij}^{(n)} = a_{ij}u_j^{(n)}$ in (28) and its corresponding $\tilde{d}_j^{L,(n)}$ in (29) are a choice that minimizes $\sum_{j=1}^{N_p} (u_j^{(n)})^2 d_j^{L,(n)}$ among all possible $d_j^{L,(n)}$ in (19), i.e.,

$$\{\tilde{\lambda}_{ij}^{(n)}\} = \arg \min_{\{\lambda_{ij}^{(n)}\}} \sum_{j=1}^{N_p} (u_j^{(n)})^2 \left(\sum_{\substack{i=1 \\ a_{ij} \neq 0}}^{N_d} \tilde{c}_i^{(n)} \frac{a_{ij}^2}{\lambda_{ij}^{(n)}} \sum_{\substack{l=1 \\ a_{il} \neq 0}}^{N_p} \lambda_{il}^{(n)} \right)$$

subject to the positivity constraint on $\lambda_{ij}^{(n)}$ if $a_{ij} \neq 0$.

Proof: By the Schwarz inequality $\langle \mathbf{s}, \mathbf{t} \rangle^2 \leq \|\mathbf{s}\|^2 \|\mathbf{t}\|^2$, we have

$$\left(\sum_{\substack{j=1 \\ a_{ij} \neq 0}}^{N_p} a_{ij} u_j^{(n)} \right)^2 \leq \sum_{\substack{j=1 \\ a_{ij} \neq 0}}^{N_p} (u_j^{(n)})^2 \frac{a_{ij}^2}{\lambda_{ij}^{(n)}} \sum_{\substack{l=1 \\ a_{il} \neq 0}}^{N_p} \lambda_{il}^{(n)}$$

where

$$s_j = \sqrt{\lambda_{ij}^{(n)} / \sum_{l=1}^{N_p} \lambda_{il}^{(n)}}$$

and

$$t_j = a_{ij} u_j^{(n)} \sqrt{\sum_{l=1}^{N_p} \lambda_{il}^{(n)} / \lambda_{ij}^{(n)}}.$$

Then

$$\begin{aligned} & \sum_{j=1}^{N_p} (u_j^{(n)})^2 d_j^{L,(n)} \\ &= \sum_{i=1}^{N_d} \tilde{c}_i^{(n)} \left(\sum_{\substack{j=1 \\ a_{ij} \neq 0}}^{N_p} (u_j^{(n)})^2 \frac{a_{ij}^2}{\lambda_{ij}^{(n)}} \sum_{\substack{l=1 \\ a_{il} \neq 0}}^{N_p} \lambda_{il}^{(n)} \right) \\ &\geq \sum_{i=1}^{N_d} \tilde{c}_i^{(n)} \left(\sum_{\substack{j=1 \\ a_{ij} \neq 0}}^{N_p} a_{ij} u_j^{(n)} \right)^2 \\ &= \sum_{j=1}^{N_p} \left(\sum_{\substack{i=1 \\ a_{ij} \neq 0}}^{N_d} \tilde{c}_i^{(n)} a_{ij} u_j^{(n)} \sum_{\substack{l=1 \\ a_{il} \neq 0}}^{N_p} a_{il} u_l^{(n)} \right) \end{aligned}$$

$$\begin{aligned}
 &= \sum_{j=1}^{N_p} \left(u_j^{(n)} \right)^2 \left(\frac{1}{u_j^{(n)}} \sum_{\substack{i=1 \\ a_{ij} \neq 0}}^{N_d} \check{c}_i^{(n)} a_{ij} \sum_{\substack{l=1 \\ a_{il} \neq 0}}^{N_p} a_{il} u_l^{(n)} \right) \\
 &= \sum_{j=1}^{N_p} \left(u_j^{(n)} \right)^2 \tilde{d}_j^{L,(n)}.
 \end{aligned}$$

APPENDIX B

OUTLINE OF THE PROPOSED NU-OS-SQS ALGORITHM

Set M , n_{end} , n_{loop} and initialize x by an FBP image. Generate u_j from an FBP image by edge and intensity detectors. Compute the maximum curvature $\check{c}_i = \max \{ \check{h}_i(0), \eta \}$. $d_j^L = 0$, $\gamma_j = 0$, $x_{j,\text{ref}} = x_j$, and the final image $\bar{x}_j = 0$.

$$\tilde{d}_j^R = \frac{1}{u_j} \sum_{k=1}^{N_r} \check{\psi}_k(0) |c_{kj}| \left(\sum_{l=1}^{N_p} |c_{kl}| u_l \right) \quad (50)$$

$n = 0$

for $m = 0, 1, \dots, M - 1$

$$\begin{aligned}
 d_{j,\text{sub}}^L &= \frac{1}{u_j} \sum_{i \in S_m} \check{c}_i a_{ij} \left(\sum_{l=1}^{N_p} a_{il} u_l \right) \\
 d_j^L &+= d_{j,\text{sub}}^L \quad \text{and} \quad \gamma_j &+= I_{\{d_{j,\text{sub}}^L > 0\}}
 \end{aligned} \quad (51)$$

end

for $n = 1, 2, \dots, n_{\text{end}} - 1$

if $n \bmod n_{\text{loop}} = 1$ and $n \leq n_{\text{fix}}$

$$\tilde{d}_j^L = d_j^L, \quad \text{and computed } \tilde{d}_j^R \text{ by (50)}$$

elseif $n \bmod n_{\text{loop}} = n_{\text{loop}} - 1$ and $n \leq n_{\text{fix}} - 2$

$$x_{j,\text{ref}} = x_j$$

elseif $n \bmod n_{\text{loop}} = 0$ and $n \leq n_{\text{fix}} - 1$

$$d_j^L = 0, \quad \text{and } u_j = g(F_{\text{cdf}}(x_j - x_{j,\text{ref}}))$$

end

for $m = 0, 1, \dots, M - 1$

$$x_{j,\text{prev}} = x_j$$

if $n \bmod n_{\text{loop}} \neq 0$ or $n \geq n_{\text{fix}}$

$$g_{j,\text{sub}}^L = \frac{\partial}{\partial x_j} L_m(x_{\text{prev}}) \quad (52)$$

else

compute both $d_{j,\text{sub}}^L$ by (51) and $g_{j,\text{sub}}^L$ by (52) simultaneously using two-input projection function, and

$$d_j^L &+= d_{j,\text{sub}}^L$$

end

$$x_j = \left[x_{j,\text{prev}} - \frac{\gamma_j g_{j,\text{sub}}^L + \frac{\partial}{\partial x_j} R(x_{\text{prev}})}{d_j^L + \tilde{d}_j^R} \right]_+ \quad (53)$$

if $n = n_{\text{end}} - 1$

$$\bar{x}_j = \frac{m}{m+1} \bar{x}_j + \frac{1}{m+1} x_j$$

end

end

end

ACKNOWLEDGMENT

D. Kim would like to thank S. Ramani for suggesting Lemma 1. J. A. Fessler acknowledges helpful discussions with J. Nuyts about the denominators for OS methods. The authors would like to thank anonymous reviewers for their valuable comments.

REFERENCES

- [1] H. Erdogan and J. A. Fessler, "Monotonic algorithms for transmission tomography," *IEEE Trans. Med. Imag.*, vol. 18, no. 9, pp. 801–814, Sep. 1999.
- [2] I. A. Elbakri and J. A. Fessler, "Statistical image reconstruction for polyenergetic X-ray computed tomography," *IEEE Trans. Med. Imag.*, vol. 21, no. 2, pp. 89–99, Feb. 2002.
- [3] J. A. Fessler, "Statistical image reconstruction methods for transmission tomography," in *Handbook of Medical Imaging*, M. Sonka and J. M. Fitzpatrick, Eds. Bellingham, WA: SPIE, 2000, vol. 2, pp. 1–70.
- [4] J.-B. Thibault, K. Sauer, C. Bouman, and J. Hsieh, "A three-dimensional statistical approach to improved image quality for multi-slice helical CT," *Med. Phys.*, vol. 34, no. 11, pp. 4526–4544, Nov. 2007.
- [5] J.-B. Thibault, C. A. Bouman, K. D. Sauer, and J. Hsieh, "A recursive filter for noise reduction in statistical iterative tomographic imaging," *Proc. SPIE Computat. Imag. IV*, p. 60650X, 2006.
- [6] K. Sauer and C. Bouman, "A local update strategy for iterative reconstruction from projections," *IEEE Trans. Signal Process.*, vol. 41, no. 2, pp. 534–548, Feb. 1993.
- [7] Z. Yu, J.-B. Thibault, C. A. Bouman, K. D. Sauer, and J. Hsieh, "Fast model-based X-ray CT reconstruction using spatially non-homogeneous ICD optimization," *IEEE Trans. Image Process.*, vol. 20, no. 1, pp. 161–175, Jan. 2011.
- [8] G. H. Golub and C. F. Van Loan, *Matrix Computations*, 2 ed. Baltimore, MD: Johns Hopkins Univ. Press, 1989.
- [9] D. Kim, "Axial block coordinate descent (ABCD) algorithm for X-ray CT image reconstruction," *Proc. Int. Meeting Fully 3-D Image Reconstruct. Radiol. Nucl. Med.*, pp. 262–265, 2011.
- [10] T. M. Benson, B. K. B. D. Man, L. Fu, and J.-B. Thibault, "Block-based iterative coordinate descent," in *Proc. IEEE Nucl. Sci. Symp. Med. Imag. Conf.*, 2010, pp. 2856–2859.
- [11] J. A. Fessler, E. P. Ficaro, N. H. Clinthorne, and K. Lange, "Grouped-coordinate ascent algorithms for penalized-likelihood transmission image reconstruction," *IEEE Trans. Med. Imag.*, vol. 16, no. 2, pp. 166–175, Apr. 1997.

- [12] B. De Man, S. Basu, J.-B. Thibault, J. Hsieh, J. A. Fessler, C. Bouman, and K. Sauer, "A study of different minimization approaches for iterative reconstruction in X-ray CT," in *Proc. IEEE Nucl. Sci. Symp. Med. Imag. Conf.*, 2005, vol. 5, pp. 2708–2710.
- [13] H. M. Hudson and R. S. Larkin, "Accelerated image reconstruction using ordered subsets of projection data," *IEEE Trans. Med. Imag.*, vol. 13, no. 4, pp. 601–609, Dec. 1994.
- [14] H. Erdogan and J. A. Fessler, "Ordered subsets algorithms for transmission tomography," *Phys. Med. Biol.*, vol. 44, no. 11, pp. 2835–2851, Nov. 1999.
- [15] J. Nuyts, B. D. Man, P. Dupont, M. Defrise, P. Suetens, and L. Mortelmans, "Iterative reconstruction for helical CT: A simulation study," *Phys. Med. Biol.*, vol. 43, no. 4, pp. 729–737, Apr. 1998.
- [16] J. A. Fessler and S. D. Booth, "Conjugate-gradient preconditioning methods for shift-variant PET image reconstruction," *IEEE Trans. Image Process.*, vol. 8, no. 5, pp. 688–699, May 1999.
- [17] T. Goldstein and S. Osher, "The split Bregman method for L1-regularized problems," *SIAM J. Imag. Sci.*, vol. 2, no. 2, pp. 323–343, 2009.
- [18] S. Ramani and J. A. Fessler, "A splitting-based iterative algorithm for accelerated statistical X-ray CT reconstruction," *IEEE Trans. Med. Imag.*, vol. 31, no. 3, pp. 677–688, Mar. 2012.
- [19] K. Lange, D. R. Hunter, and I. Yang, "Optimization transfer using surrogate objective functions," *J. Computat. Graph. Stat.*, vol. 9, no. 1, pp. 1–20, Mar. 2000.
- [20] M. W. Jacobson and J. A. Fessler, "An expanded theoretical treatment of iteration-dependent majorize-minimize algorithms," *IEEE Trans. Image Process.*, vol. 16, no. 10, pp. 2411–2422, Oct. 2007.
- [21] D. Kim and J. A. Fessler, "Parallelizable algorithms for X-ray CT image reconstruction with spatially non-uniform updates," *Proc. 2nd Int. Meeting Image Formation X-ray CT*, pp. 33–36, 2012.
- [22] D. P. Bertsekas, "A new class of incremental gradient methods for least squares problems," *SIAM J. Optim.*, vol. 7, no. 4, pp. 913–926, Nov. 1997.
- [23] A. Nedic and D. P. Bertsekas, "Incremental subgradient methods for nondifferentiable optimization," *SIAM J. Optim.*, vol. 12, no. 1, pp. 109–138, 2001.
- [24] C. L. Byrne, "Block-iterative methods for image reconstruction from projections," *IEEE Trans. Image Process.*, vol. 5, no. 5, pp. 792–793, May 1996.
- [25] S. Ahn and J. A. Fessler, "Globally convergent image reconstruction for emission tomography using relaxed ordered subsets algorithms," *IEEE Trans. Med. Imag.*, vol. 22, no. 5, pp. 613–626, May 2003.
- [26] S. Ahn, J. A. Fessler, D. Blatt, and A. O. Hero, "Convergent incremental optimization transfer algorithms: Application to tomography," *IEEE Trans. Med. Imag.*, vol. 25, no. 3, pp. 283–296, Mar. 2006.
- [27] G. I. Angelis, A. J. Reader, F. A. Kotassidis, W. R. Lionheart, and J. C. Matthews, "The performance of monotonic and new non-monotonic gradient ascent reconstruction algorithms for high-resolution neuroreceptor PET imaging," *Phys. Med. Biol.*, vol. 56, no. 13, pp. 3895–3917, Jul. 2011.
- [28] M. Defrise, F. Noo, and H. Kudo, "A solution to the long-object problem in helical cone-beam tomography," *Phys. Med. Biol.*, vol. 45, no. 3, pp. 623–643, Mar. 2000.
- [29] D. Kim, D. Pal, J.-B. Thibault, and J. A. Fessler, "Improved ordered subsets algorithm for 3-D X-ray CT image reconstruction," *Proc. 2nd Int. Meeting Image Format. X-ray CT*, pp. 378–381, 2012.
- [30] M. Yavuz and J. A. Fessler, "Statistical image reconstruction methods for randoms-precorrected PET scans," *Med. Image Anal.*, vol. 2, no. 4, pp. 369–378, Dec. 1998.
- [31] J. M. Ortega and W. C. Rheinboldt, *Iterative Solution of Nonlinear Equations in Several Variables*. New York: Academic, 1970.
- [32] P. J. Huber, *Robust Statistics*. New York: Wiley, 1981.
- [33] A. P. Dempster, N. M. Laird, and D. B. Rubin, "Maximum likelihood from incomplete data via the EM algorithm," *J. R. Stat. Soc. Ser. B*, vol. 39, no. 1, pp. 1–38, 1977.
- [34] A. R. D. Pierro, "On the convergence of the iterative image space reconstruction algorithm for volume ECT," *IEEE Trans. Med. Imag.*, vol. 6, no. 2, pp. 174–175, Jun. 1987.
- [35] A. R. D. Pierro, "On the relation between the ISRA and the EM algorithm for positron emission tomography," *IEEE Trans. Med. Imag.*, vol. 12, no. 2, pp. 328–333, Jun. 1993.
- [36] A. R. D. Pierro, "A modified expectation maximization algorithm for penalized likelihood estimation in emission tomography," *IEEE Trans. Med. Imag.*, vol. 14, no. 1, pp. 132–137, Mar. 1995.
- [37] K. Lange and J. A. Fessler, "Globally convergent algorithms for maximum a posteriori transmission tomography," *IEEE Trans. Image Process.*, vol. 4, no. 10, pp. 1430–1438, Oct. 1995.
- [38] I. Daubechies, M. Defrise, and C. D. Mol, "An iterative thresholding algorithm for linear inverse problems with a sparsity constraint," *Comm. Pure Appl. Math.*, vol. 57, no. 11, p. 1413, Nov. 2004.
- [39] A. Beck and M. Teboulle, "A fast iterative shrinkage-thresholding algorithm for linear inverse problems," *SIAM J. Imag. Sci.*, vol. 2, no. 1, pp. 183–202, 2009.
- [40] S. Sothivirat and J. A. Fessler, "Image recovery using partitioned-separable paraboloidal surrogate coordinate ascent algorithms," *IEEE Trans. Image Process.*, vol. 11, no. 3, pp. 306–317, Mar. 2002.
- [41] D. Kim and J. A. Fessler, "Accelerated ordered-subsets algorithm based on separable quadratic surrogates for regularized image reconstruction in X-ray CT," in *Proc. IEEE Int. Symp. Biomed. Imag.*, 2011, pp. 1134–1137.
- [42] J. A. Fessler, N. H. Clinthorne, and W. L. Rogers, "On complete data spaces for PET reconstruction algorithms," *IEEE Trans. Nucl. Sci.*, vol. 40, no. 4, pp. 1055–1061, Aug. 1993.
- [43] Y. Long, J. A. Fessler, and J. M. Balter, "3-D forward and back-projection for X-ray CT using separable footprints," *IEEE Trans. Med. Imag.*, vol. 29, no. 11, pp. 1839–1850, Nov. 2010.
- [44] J. H. Cho and J. A. Fessler, "Accelerating ordered-subsets image reconstruction for X-ray CT using double surrogates," *Proc. SPIE Med. Imag.*, p. 83131X, 2012.
- [45] Z. Q. Luo, "On the convergence of the LMS algorithm with adaptive learning rate for linear feedforward networks," *Neural Computat.*, vol. 3, no. 2, pp. 226–245, Jun. 1991.
- [46] A. H. Delaney and Y. Bresler, "Globally convergent edge-preserving regularized reconstruction: an application to limited-angle tomography," *IEEE Trans. Image Process.*, vol. 7, no. 2, pp. 204–221, Feb. 1998.
- [47] R. C. Fair, "On the robust estimation of econometric models," *Ann. Econ. Social Measur.*, vol. 2, pp. 667–677, Oct. 1974.
- [48] J. A. Fessler and W. L. Rogers, "Spatial resolution properties of penalized-likelihood image reconstruction methods: Space-invariant tomographs," *IEEE Trans. Image Process.*, vol. 5, no. 9, pp. 1346–1358, Sep. 1996.
- [49] L. Yu, Y. Zou, E. Y. Sidky, C. A. Pelizzari, P. Munro, and X. Pan, "Region of interest reconstruction from truncated data in circular cone-beam CT," *IEEE Trans. Med. Imag.*, vol. 25, no. 7, pp. 869–881, Jul. 2006.

Accelerating ordered subsets image reconstruction for X-ray CT using spatially non-uniform optimization transfer: Supplementary material

Donghwan Kim, *Student Member, IEEE*, Debashish Pal, *Member, IEEE*, Jean-Baptiste Thibault, *Member, IEEE*, and Jeffrey A. Fessler, *Fellow, IEEE*

This material extends the result section of [1] by providing cost function plots and a simulation study of a helical scan of the XCAT phantom [2].

References to equations, tables, figures, bibliography are within this material unless they are specified.

I. COST FUNCTION

In [1], we computed root mean square difference (RMSD) within region-of-interest (ROI) to evaluate the convergence rate of the proposed algorithm. Another way to assess the convergence rate is computing the cost function $\Psi(x)$ in [1, Eqn. (2)] at each iteration. We used the following metric:

$$\xi^{(n)} = 20 \log_{10} \left(\frac{\Psi(x^{(n)}) - \Psi(x^{(\infty)})}{\Psi(x^{(\infty)})} \right) \text{ [dB]} \quad (1)$$

to better visualize how the cost function decreases each iteration. We used double precision and triple **for** loops when accumulating $\Psi(x^{(n)})$ to ensure high accuracy.

Fig. 2 shows plots of $\xi^{(n)}$ for the choices of parameters used in [1, Fig. 5 and 6] for two real 3D scans; GE performance phantom (GEPP) and shoulder region scan. Fig. 2(a) shows that for the GEPP case, the NU-OS methods decreased the cost function at about the same rate than the ordinary OS method, or even perhaps slightly slower. In contrast, when we plotted RMSD distance to the converged image within the ROI [1, Fig. 5], NU-OS converged significantly faster. The reason for this different behavior is that the cost function plot considers all voxels, even those outside the ROI which are not of interest clinically. It is known that OS methods are not guaranteed to converge and apparently the non-ROI voxels are either not converging or perhaps approaching a larger limit-cycle, presumably due to the poor sampling in the padded slices outside the ROI, even with the stabilizing methods outside ROI described in [1, Section V]. Therefore, cost function plots may not provide practical measures of convergence rate for OS methods, particularly with acceleration. Future research on

trying to further stabilize the NU-OS-SQS algorithm outside the ROI also may be helpful.

The final drops at the right in Fig. 2(a) show that averaging sub-iterations at the last iteration, as described in [1, Section IV.C], can compensate for the limit-cycle, particularly outside the ROI.

Unlike Fig. 2(a), the plots in Fig. 2(b) and 2(c) of shoulder region scan look similar to the plots of RMSD within ROI in [1, Fig. 6]. The scan geometry of each data set might explain these behavior of cost function in Fig. 2, where the shoulder region scan is a helical scan with pitch 1.0 and 7 helical turns and thus the corresponding image space has relatively few voxels outside the ROI, compared with GEPP data that is acquired by a helical scan with pitch 0.5 and 3 helical turns. Therefore, we can expect the cost function of shoulder region scan to be less affected by instability outside the ROI. Slower convergence of NU-OS-SQS algorithm at early iterations in Fig. 2(c) means that some choices of initial update-needed factor $\tilde{u}_j^{(0)}$ were not good enough for voxels outside the ROI. The effect of averaging at the last iterations is apparent in Fig. 2(b) and 2(c), because the instability outside the ROI is suppressed by the averaging.

II. SIMULATION DATA

A. Simulation data

We simulated a helical CT scan data by using XCAT phantom [2]. We first acquired a $1024 \times 1024 \times 154$ XCAT phantom for 500 [mm] transaxial field-of-view (FOV) at 70 [keV], where $\Delta_x = \Delta_y = 0.4883$ [mm] and $\Delta_z = 0.6250$ [mm]. (See Fig. 1.)

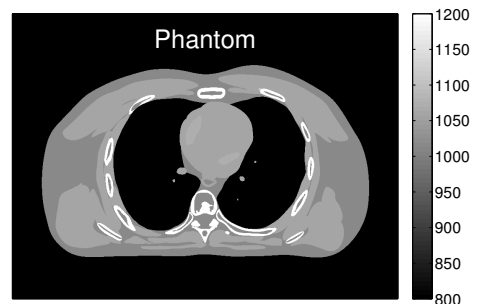


Fig. 1. A simulated XCAT phantom: a center slice of $1024 \times 1024 \times 154$ XCAT phantom. (Images are cropped for better visualization.)

Date of current version June 4, 2013. This work was supported in part by GE Healthcare, the National Institutes of Health under Grant R01-HL-098686, and equipment donations from Intel.

Donghwan Kim and Jeffrey A. Fessler are with the Department of Electrical Engineering and Computer Science, University of Michigan, Ann Arbor, MI 48105 USA (e-mail: kimdongh@umich.edu, fessler@umich.edu).

Debashish Pal and Jean-Baptiste Thibault are with GE Healthcare Technologies, 3000 N Grandview Blvd, W-1180, Waukesha, WI 53188 USA (e-mail: debashish.pal@ge.com, jean-baptiste.thibault@med.ge.com).

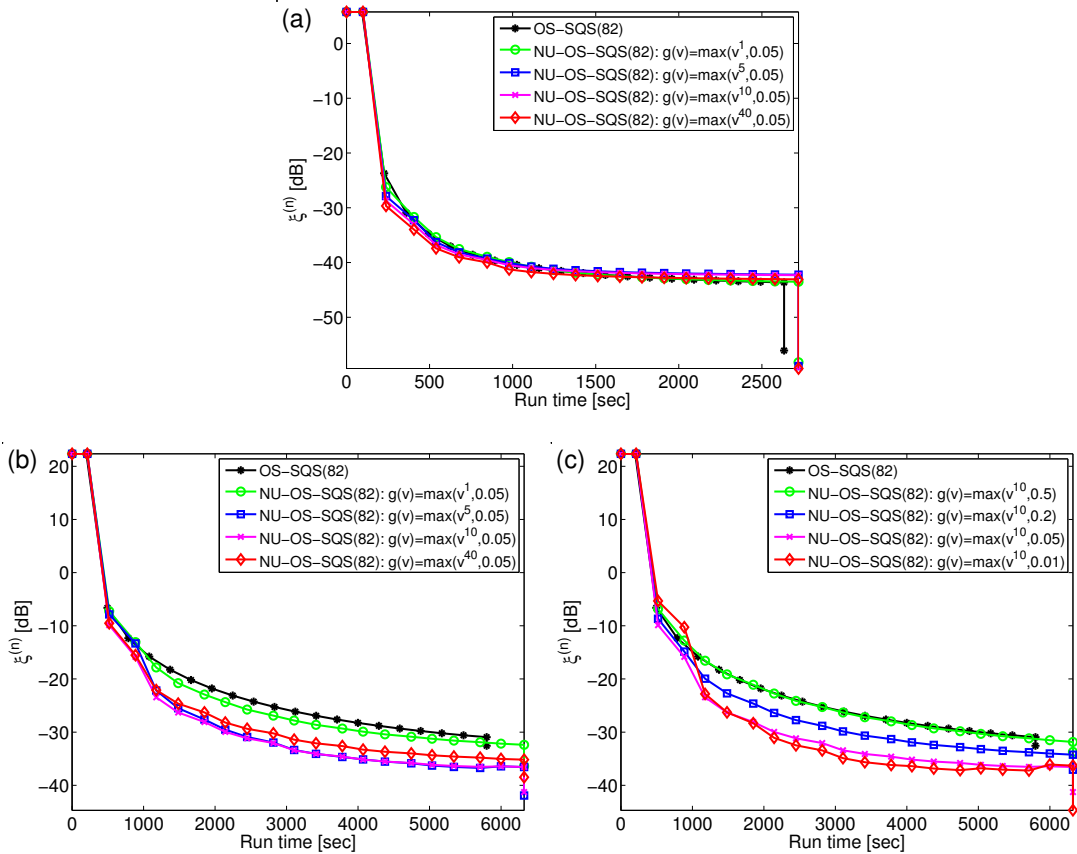


Fig. 2. Plots of $\xi^{(n)}$ in (1) as a function of run time for different choice of DRA parameters for (a) GE performance phantom and (b-c) a shoulder region scan.

We simulated a helical scan using the blank scan factor $b_i = 10^6$ and the mean number of background events $r_i = 0$ with Poisson noise. The sinogram data is in $888 \times 64 \times 2934$ (the number of detector columns \times detector rows \times projection views) space with pitch 1.0. Then, we reconstructed a $512 \times 512 \times 154$ image where $\Delta_x = \Delta_y = 0.9766[\text{mm}]$ and $\Delta_z = 0.6250[\text{mm}]$ using the proposed NU-OS-SQS algorithm.

B. Results

We use a cost function that is similar to the cost function used in [1, Section V]. We solve a PWLS function with a potential function $\psi_k(t) \triangleq \bar{\omega}_k \psi(t)$ in [1, Eqn. (45)] using a spatial weighting parameter:

$$\bar{\omega}_k \triangleq 50 \cdot \prod_{\substack{j=1 \\ c_{k,j} \neq 0}}^{N_p} \max\{\kappa_j, 0.01 \kappa_{\max}\} \quad (2)$$

that provides uniform resolution properties [3], where

$$\kappa_j \triangleq \sqrt{\frac{\sum_{i=1}^{N_d} a_{ij} w_i}{\sum_{i=1}^{N_d} a_{ij}}} \quad (3)$$

and the value of $\kappa_{\max} \triangleq \max_j \kappa_j$ is used in (2) to avoid under-regularizing some voxels with very small κ_j . Fig. 3 illustrates

both RMSD within ROI and $\xi^{(n)}$ versus computation time, which we run the algorithm on the machine described in [1].

In Fig. 3(a), we evaluated the convergence rate using RMSD within ROI between current and converged image, where the converged image was generated by many iterations of a (convergent) SQS. We used parameters of DRA function that are used in [1, Fig. 5 and 6], and we observed similar trends. We also illustrate the plot of $\xi^{(n)}$ versus run time in Fig. 3(b), which looks very similar to Fig. 3(a). This is because we regularized relatively more than two other experiments in this simulation experiment, and thus instability outside the ROI that can be caused by NU-OS-SQS methods is not apparent here.

In Fig. 4(a), the reconstructed images of (NU)-OS-SQS show that NU method accelerates OS-SQS and reaches closer to the converged image after the same computation time (88 min.). This is apparent when comparing the difference images between the reconstructed and converged images in Fig. 4(b), particularly around the spine.

REFERENCES

- [1] D. Kim, D. Pal, J-B. Thibault, and J. A. Fessler, "Accelerating ordered subsets image reconstruction for X-ray CT using spatially non-uniform optimization transfer," *IEEE Trans. Med. Imag.*, 2013, To appear.
- [2] W. P. Segars, M. Mahesh, T. J. Beck, E. C. Frey, and B. M. W. Tsui, "Realistic CT simulation using the 4D XCAT phantom," *Med. Phys.*, vol. 35, no. 8, pp. 3800–8, Aug. 2008.

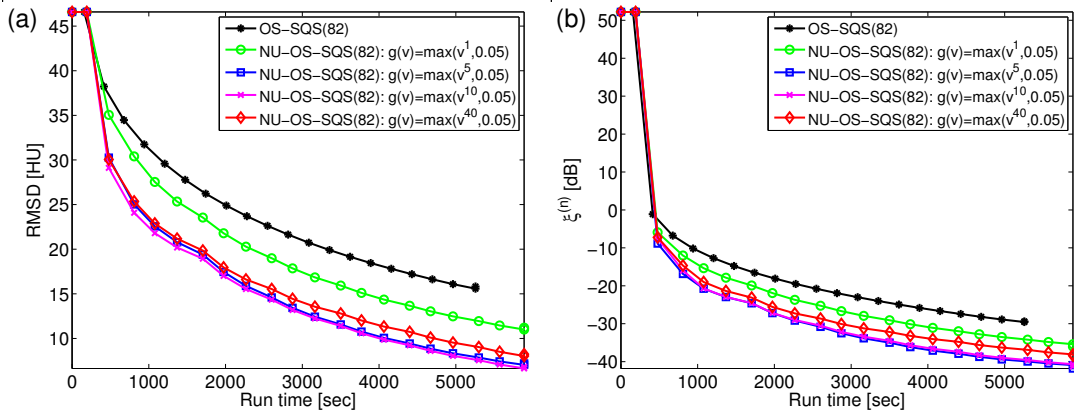


Fig. 3. A simulated XCAT phantom: plots of (a) RMSD and (b) $\xi^{(n)}$ versus run time for different choice of parameters t for $\epsilon = 0.05$ in $g(v) = \max\{v^t, \epsilon\}$.

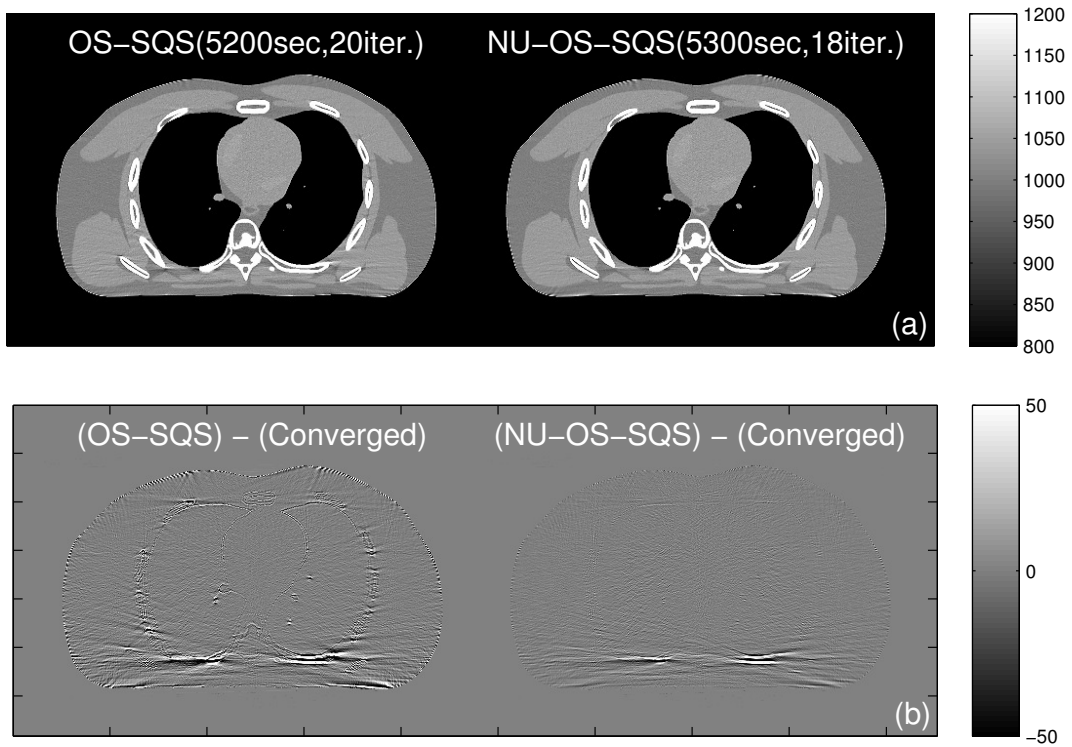


Fig. 4. A simulated XCAT phantom: (a) A center slice of reconstructed image by OS-SQS(82) and NU-OS-SQS(82)- $g(v) = \max\{v^{10}, 0.05\}$ after about 88 min. (b) Difference between the reconstructed and converged images are additionally shown to illustrate the acceleration of NU approach. (Images are cropped for better visualization.)

[3] J. A. Fessler and W. L. Rogers, "Spatial resolution properties of penalized-likelihood image reconstruction methods: Space-invariant tomographs," *IEEE Trans. Im. Proc.*, vol. 5, no. 9, pp. 1346–58, Sept. 1996.